
Università degli Studi di Palermo

**DIPARTIMENTO DI FISICA E CHIMICA**
**DOTTORATO DI RICERCA IN FISICA – XXVI CICLO**

# Fine structure and dynamic heating from temporal and spatial analysis of a solar active region observed with Solar Dynamics Observatory (SDO)

**Edris Tajfirouze**

Palermo, November 2015

Supervisore: Prof. Fabio Reale

# Abstract

An outstanding issue in current solar and astrophysical research is that of the heating of the solar corona. How is the corona heated to temperatures of greater than 1 MK when the photosphere below is only 6000 K? One observational approach to addressing this important question is to focus on particular areas in the corona such as active regions (ARs). In a scenario that heating is impulsive and the cross-field spatial scale of the heating is so small, under the resolution of the current instruments, we attempted to narrow the question further to discrete bright magnetic flux tubes, the coronal loops, inside active regions. We investigate the emission variability, heating and substructure of coronal loops in the core of one such active region, observed in high spatial and temporal detail by the Solar Dynamics Observatory (SDO) in 2010. Widespread in that active region, previous works had detected small amounts of very hot plasma ($> 4$ MK), much hotter than the typical plasma temperature of coronal plasma in active regions ($\sim 3$ MK), outside of major flares. Most probably, storms of fast and intense heat pulses bring some plasma to such high temperature for a short time, and the work in this thesis develops under this scenario of highly intermittent heating, and is divided into two parts.

In the first part, our approach is to analyze single light curves in the smallest resolution elements (0.6") of the images taken in two EUV channels (94 Å and 335 Å) with a high cadence ($\sim 12$ s) from the Atmospheric Imaging Assembly on-board SDO. We compare the observed light curves with those obtained from a specific loop model. According to the model, a loop is made up of a bundle of thinner strands, each heated impulsively and independently of the others. The frequency of the pulses depends on their energy as a power-law, more intense ones being also less frequent. The pulses occur at random times. We use a 0D strand hydrodynamic model, which describes the evolution of the space-averaged physical quantities, in particular density and temperature, and from them we derive the EUV light curves in a single strand. We then combine the light curves of many single strands that we would intercept along the line of sight inside a pixel.

The next step is to compare the resulting simulated light curves with the observed light curves. We use two independent methods: an artificial intelligent system (Probabilistic Neural Network, PNN) and a simple cross-correlation technique. We make some exploration of the space of the parameters to constrain the distribution of the heat pulses, their duration and their spatial size, and, as a feedback on the data, their signatures on the light curves. From both methods the best agreement is obtained for a relatively large population of events (1000) with a short duration (less than 1 minute) and a relatively shallow distribution (power law with index 1.5) in a limited energy range (1.5 decades). The feedback on the data indicates that bumps in the light curves, especially in the 94 Å channel, are signatures of a heating excess that occurred a few minutes before.

In the second part of the work we extend the analysis of time resolved emission of single pixels by including spatially resolved strand modeling and by studying the evolution of emission along the loops in the EUV 94 Å and 335 Å channels. We replicate the modeling using a 1D hydrodynamic code that describes the evolution of the physical quantities distributed along the loop strand. We use exactly the same parameters which labeled the best absolute match in the first part, as the input of the space-resolved analysis. We find that the amplitude of the random fluctuations driven by the random heat pulses increases from the bottom to the top of the loop in the 94 Å channel and, viceversa, from the top to the bottom in the 335 Å channel. This prediction is confirmed by the observation of a set of aligned neighbouring pixels along a bright arc of an active region core. Maps of pixel fluctuations may therefore provide easy diagnostics of nano-flaring regions.

# Acknowledgements

First and foremost I would like to appreciate largely my kind supervisor, Prof. Fabio Reale who taught me eagerly and patiently during my Ph.D. program. I have been extremely lucky to have a supervisor who cared so much about my work, and who responded to my questions and queries so promptly. I want to thank my friend Antonino Petralia. He has taught me, both consciously and un-consciously, how good experimental physics is done. I appreciate all his contributions of time, ideas, and suggestions to make my Ph.D. experience productive and stimulating. He always encouraged me to be patient and to stay calm. The members of the Osservatorio Astronomico Di Palermo (OAPA) institute are really appreciated. They were very kind to me. Special thanks to Flavio Morale the Computer Technician at the OAPA who helped me technically and prompted me to speed up. The group has been a source of friendships as well as good advice and collaborations.

I would like to acknowledge honorary my Co-authors, specially Paola Testa from Harvard-Smithsonian Center for Astrophysics for her useful suggestions data preparations and hearty collaborations.

I gratefully acknowledge the funding source that made my Ph.D. work possible. I was funded by the university of Palermo/Italy during my 3 years Ph.D program.

Lastly, I would like to thank my family for all their love and encouragement. For my parents and mostly my sisters as well as my uncle who raised me with a love of science and supported me in all my pursuits.

# Contents

# Chapter 1

# Introduction

## 1.1 Solar corona

The solar corona is the outer atmosphere of the sun. Compared to its underlying atmospheres it is tenuous, therefore in optical band and through solar eclipse one can see a faintly colored luminous ring or halo (visible corona) surrounding a disk. In the solar atmosphere the temperature increases very steeply from 6000 degrees to a few million degrees in the corona, in a range 500 kilometers above the photosphere. Thus, the outer atmosphere of the Sun, the corona, is indeed hotter than the underlying photosphere, and specific local sources of energy release must be invoked.

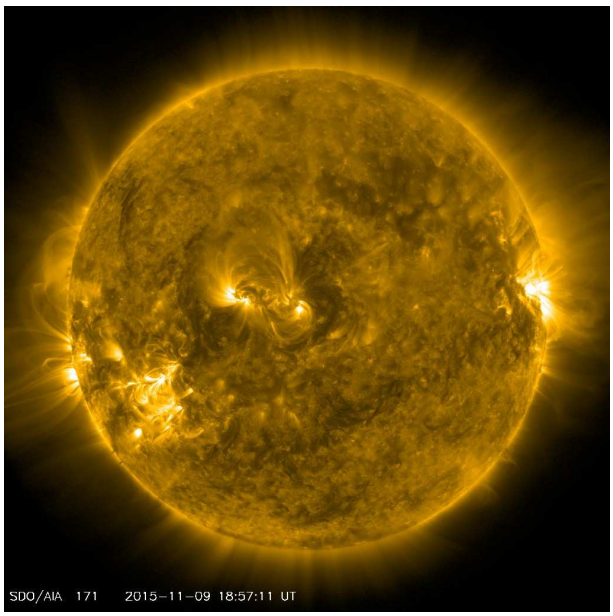


**Figure 1.1:** Full Disk image of the sun taken by Solar Dynamic Observatory (SDO) in Extreme Ultra Violet (171 $\mathring{A}$) band, 11 September 2015. Credit: NAsa/LMSAL/SDO.

In the x-ray and EUV (Extreme Ultra Violet) band the corona is seen to be highly structured (Reidy et al. 1968; van Speybroeck et al. 1970).
The corona is fully ionized and it can efficiently interact with its ambient magnetic field, leading the corona to be highly inhomogeneous.
The decisive parameter is the ratio of thermal pressure $P_{th}$ to the magnetic pressure $P_{mag}$, also called the plasma $\beta$ parameter which is less than unity in corona. The electron density in the solar corona ranges from $\sim 10^6\, cm^{-3}$ in the upper corona (at a height of 1 solar radius) to $\sim 10^{11}\, cm^{-3}$. It is $\sim 10^{-12}$ times as dense as the photosphere. The corona can be morphologically devided into 3 main regions, which all vary their sizes during the solar cycle (solar magnetic activity cycle is the nearly periodic 11 years change in the sun's activity.) Active regions, quiet sun and coronal holes which are worth mentioning.

- Active regions: They cover areas which are brighter in the x-ray and EUV. A colony of strong magnetic field concentration is placed in this area. These ensembles of magnetic flux tubes are visible as sunspots groups in optical wavelengths or magnetograms. Because of the bipolar nature of this region, the involved magnetic field lines are mainly closed. Due to the permenent magnetic activity there, most of the solar activity like flares and Coronal Mass Ejections (CME's) is related to this area.

- Quiet sun: The remaining part out of the active region is traditionally called quiet sun. Dynamic processes in the quiet sun range from small scale phenomena such as network heating events, nanoflares, explosive events, bright points and soft x-ray jets to large scale structures such as transequatorial loops or coronal arches. Most of the large scale structures that overarch quiet sun regions are rooted in active region(Golub & Pasachoff 2009).

- Coronal holes: The northern and southern polar zones seem to be darker over the sun's image (in x-ray and EUV) due to the lower density plasma. The magnetic fields are open there and cause the plasma to erupt to the interstellar medium and to form the so-called solar winds.

## 1.2 Coronal loops

The bright corona in the x-ray and EUV band appears to be made up of arch-like structures called coronal loops (figure 1.2). They are essentially overdense structures that are filled with heated plasma.

The only available reservoir for the loop feeding is the underlying chromosphere (more dense and cool atmosphere compared to the corona) which supplies coronal loops with up-flowing plasma. Coronal loops are nothing other than conduits filled with heated plasma, shaped by the geometry of the coronal magnetic field.

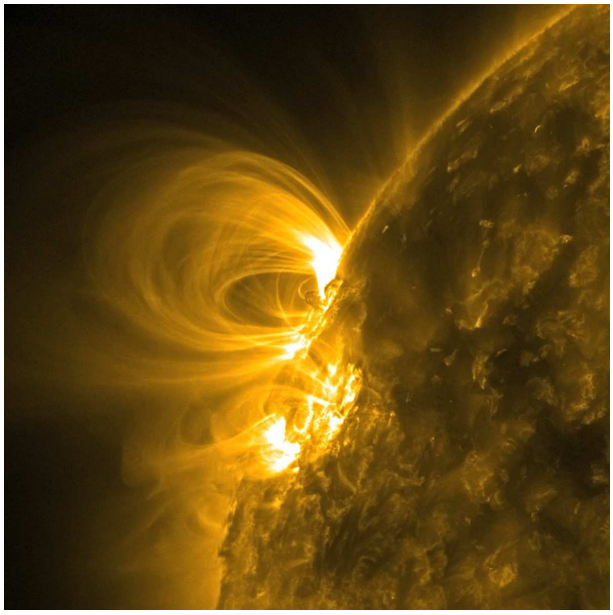

**Figure 1.2:** Coronal loops have a semicircular shape. Image: SDO/AIA, 171 Å filter, 26 February 2011. Credit: NAsa/LMSAL/SDO.

In coronal loops plasma transport occurs only in one dimension along the magnetic field lines, while the cross field diffusion is strongly inhibited. This has the consequence that every coronal loop represents a thermally isolated system, having only the tiny chromospheric footpoints as valves for rapid mass exchange.

First evidence of magnetic confinement came from rocket missions in the 1960s. In particular, in 1965, arcmin angular resolution was achieved in the X-rays with grazing incidence optics (Giacconi et al. 1965). That was the first time that the useful solar photographs have been obtained with a spectral response limited to the wavelength interval between 8 and 12 Å.

The first coronal loop structures were identified properly after a rocket launch in 1968, which provided for the first time an image of an X-ray flare (Vaiana et al. 1968), with a resolution of a few arcsec.

In 1973, the X-ray telescope S-054 on-board Skylab, resolved the coronal loops and took photographs with a maximum resolution of 2 arcsec. It was confirmed that the whole X-ray bright corona consists of magnetic loops, whose lifetime is typically much longer than the characteristic cooling times (Rosner et al. 1978).

In the same mission coronal loops were also detected in the UV band at temperatures below 1 MK, by Extreme UltraViolet (EUV) telescopes S-055 (Reeves et al. 1977) and S-082 (Tousey et al. 1977; Bartoe et al. 1977). These loops are invisible in the X-ray band and many of them depart from sunspots, appear coaxial and are progressively thinner for progressively lower temperature ions (Foukal 1975, 1976).

New observations of such cool loops were performed several years later with the Solar and Heliospheric Observatory (SoHO) mission and provided new details and confirmations.

During the later Yohkoh mission, (1991-2001, Ogawara et al. 1991) Hara et al. (1992) found first indications of plasma at 5-6 MK in active regions with the Soft X-ray Telescope (SXT, Tsuneta et al. 1991).

Normal-incidence optics were developed in the late 1980s. An early experiment was the Normal Incidence X-ray Telescope (NIXT, Golub & Herant 1989), which provided a few high resolution coronal images in the EUV band.

Later space missions dedicated to study the corona have been the Solar and Heliospheric Observatory (SoHO, Domingo et al. 1995), launched in 1995 and still operative, and the Transition Region and Coronal Explore (TRACE, Handy et al. 1999) launched in 1998 and replaced in 2010 by the Solar Dynamic Observatory (SDO) instruments. Both SoHO and TRACE were tailored to observe the quiet corona (below 2 MK). SoHO images the whole corona (Extreme ultraviolet Imaging Telescope, EIT, Delaboudinière et al. 1995) and performs wide band spectroscopy (Solar Ultraviolet Measurements of Emitted Radiation, SUMER, Wilhelm et al. 1995) and (Coronal Diagnostic Spectrometer, CDS Harrison et al. 1995) in the EUV band; TRACE imaged the EUV corona with high spatial (0.5 arcsec) and temporal (30 s) resolution. Both SoHO/EIT and TRACE are based on normal-incidence optics and contain three different EUV filters that provide limited thermal diagnostics.

Thanks to their capabilities, both missions allowed to address finer diagnostics, in particular to investigate the fine transverse structuring of coronal loops, both in its geometric and thermal components, and the plasma dynamics and the heating mechanisms at a higher level of detail.

Among other relevant missions, we mention the CORONAS series (Ignatiev et al. 1998; Oraevsky & Sobelman 2002) , with instruments like SPectroheliographIc X-Ray Imaging Telescop (SPIRIT, Zhitnik et al. 2003) REntgenovsky Spektrometr s Izognutymi Kristalam (ReSIK, Sylwester et al. 1998) and Solar Photometer in X-ray (SPHINX, Sylwester et al. 2008; Gburek et al. 2013), which have contributed to the investigation of coronal loops.

In late 2006, two other major solar missions started, namely Hinode (Kosugi et al. 2007) and the Solar TErrestrial Relations Observatory (STEREO, e.g., Kaiser et al. 2008). On- board Hinode, two instruments address particularly the study of coronal loops: the X-Ray Telescope (XRT, Golub et al. 2007) and the Extreme-ultraviolet Imaging Spectrometer (EIS, Culhane et al. 2007). Both these instruments offer considerable improvements on previous missions. The XRT has a spatial resolution of about 1 arcsec, a very low scattering and the possibility to switch among nine filters and combinations of them. EIS combines well spectral ($\sim 2\,mA$), spatial ($2\,Arcsec$) and temporal ($10\,s$) resolution to obtain accurate diagnostics of plasma dynamics and density. STEREO consists of two nearly identical observatories - one ahead of Earth

in its orbit, the other trailing behind, so it allows through, for instance, its Sun-Earth Connection Coronal and Heliospheric Investigation (SECCHI) package a first 3D reconstruction of coronal loops (Aschwanden et al. 2009; Kramar et al. 2009).

In 2010, the Solar Dynamics Observatory (SDO, Pesnell et al. 2012) mission has been launched with three instruments on-board: Atmospheric Imaging Assembly (AIA, Lemen et al. 2012; Boerner et al. 2012), EUV Variability Experiment (EVE, Woods et al. 2012), and Helioseismic and Magnetic Image (HMI, Scherrer et al. 2012). SDO observations lead to an improvement in the study of coronal-loop physics. SDO takes the full disk image of the Sun with high temporal and spatial resolution, especially with the AIA EUV normal-incidence telescope at 9 different UV and EUV channels (with a pixel size of about $0.5 arcsec$ and a cadence of $10 s$). In 2012 the sounding rocket mission High-resolution Coronal Imager (Hi-C, Cirtain et al. 2013) took images with the highest resolution photos ever of the Sun's corona ($0.2\, arcsec$) in the EUV band ($195\, \mathring{A}$).

### 1.2.1 Coronal loop classification

Coronal loops can be thermally classified as:

- Hot loops: They are tipically observed in the x-ray band, hot UV and EUV lines (e.g., Fe XVI) and channels (SDO/AIA 335 Å , see secton 1.2) and especially in active region with temperatures around or above 2 MK.

- Warm loops: They are well observed in EUV images and in most channels of SDO/AIA. The confined plasma has a temperature around 1-1.5 MK

- Cool loops: They are generally detected in UV lines at temperatures between $10^5$ K and $10^6 K$.

From the morphological point of view the loops can be classified into 3 different classes; bright points, active region loops and large scale structures (giant arches). All the main physical properties are listed in table 1.1.

**Table 1.1:** Typical X-ray coronal loop parameters

| **Type** | **Length** $10^9\, cm$ | **Temperature** MK | **density** $10^9\, cm^{-3}$ | **Pressure** $dyne\, cm^{-2}$ |
|---|---|---|---|---|
| Bright points | 0.1-1 | 2 | 5 | 3 |
| Active region | 1-10 | 3 | 1-10 | 1-10 |
| Giant arches | 10-100 | 1-2 | 0.1-1 | 0.1 |
| Flaring loops | 1-10 | $> 10$ | $> 50$ | $> 100$ |

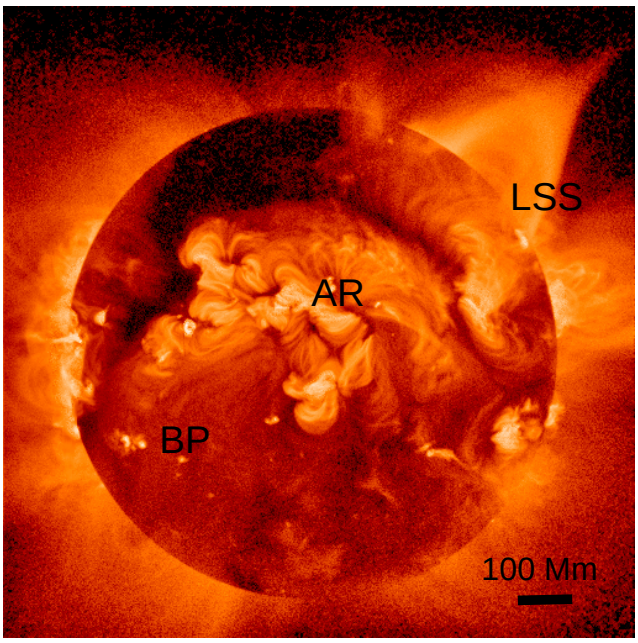


**Figure 1.3:** The X-ray corona contains loops with different spatial scales, e.g., bright points (BP), active region loops (AR), large-scale structures (LSS). The scale unit is labelled. Image credit: Yohkoh mission, ISAS, Japan.

## 1.3 Heating of the active regions

The magnetic field has been widely accepted as the main source for the extra heating in the corona. However the mechanism of converting magnetic energy into thermal energy is still unknown. It is challenging due to several difficulties such as the very efficient thermal conduction along the magnetic field lines which inhibit the determination of the localization of the heat pulses as well as the limited resolution of the current devices to resolve the elementary structures where the elementary heating events may occurs. So the recent attempts have been done through indirect evidences (Priest et al. 2000; Reale et al. 2000; Warren et al. 2003; Klimchuk 2006; Warren & Winebarger 2007; Bradshaw et al. 2012; Testa et al. 2014).

The question of heating the corona is mostly equivalent to the problem of coronal loops heating. According to Klimchuk (2006), the heating problem can be organized as follows:

- Identification of the source of the energy release.
- The mechanism of converting the energy into heat.
- The determination of the plasma response to the heating.
- predicting the spectrum of the emitted radiation.

- manifestation of heating episodes in the observable quantities.

### 1.3.1 Energy source

We can distinguish two different scenarios for the heating, the origin of both are rooted in the random motion of the photospheric footpoints driven by convective turbulences. This mechanical motion causes the magnetic field lines to be either quasi-statistically stressed or generate waves. The dissipation from the current sheets growing from magnetic stress is referred to as DC (Direct Current) heating, and the dissipation from the waves is called AC (Alternate Current) heating. It is worth pointing out that the time scale of dissipation is a critical parameter to determine if the dominant heating mechanism is wave related or reconnection related. If it is smaller than the Alfvén time scale ($t_d < t_A$) then it is very likely that the dominant heating is wave related and if not, it is most likely that the dominant heating mechanism is related with magnetic reconnection (see e.g. Walsh & Ireland 2003).

- DC heating: Random motion of photospheric footpoints does mechanical work on the coronal loop and increases its energy release at a rate given by Poynting flux through the base:

$$F = \frac{-1}{4\pi} B_\nu B_h V_h \tag{1.1}$$

  where $B_h$ and $B_\nu$ are the horizontal and vertical component of the field and $v_h$ is the horizontal footpoint velocity. The values obtained from the observations (e.g., Klimchuk 2006) show that the Poynting flux into the corona is adequate to explain the observed energy losses of both the quiet sun and active regions. However the mechanism of energy conversion from magnetic stress to heat is challenging.

- AC heating: The same mechanism stresses the magnetic field generate also upward propagating waves, like Alfvén waves, acoustic, fast and slow magnetosonic waves and so on. The real issue is whether the coronal waves may carry sufficient amount of energy flux to heat the coronal plasma. The problem is that only a small fraction of the flux carried by the waves is able to penetrate the corona and most of them are dumped passing the very steep density and temperature gradients of the chromosphere and transition region [1]. For instance the acoustic and slow mode waves form shocks and are highly damped. The fast mode waves are also strongly refracted and reflected (Narain & Ulmschneider 1996). Alfvén waves can travel a long distance without damping considerably and are able to penetrate the corona, but they are unable to supply sufficient amount of flux needed to power the corona.

[1] The transition region is a thin and very irregular layer of the Sun's atmosphere that separates the hot corona from the much cooler atmosphere

For each of the two models group (AC and DC) there are a number of variants of how the currents are dissipated, either by ohmic dissipation, magnetic reconnection, current cascading and viscose turbulence in the case of DC model, or by Alfvén resonance absorption, phase mixing, current layer formation and turbulence in the case of AC model.

### 1.3.2 Plasma response

How the plasma exactly responds to the heating is another fundamental problem. It affects seriously the subsequent heating processes. The study of plasma response to the heating episodes enables us to determine the state of the plasma from which the radiative signatures needed for testing any coronal heating theory can be explored. The response of the plasma conceptually connects the corona to the underlying atmosphere from which the enhanced or decreased pressure of the coronal loop is determined. An upward or a downward flow occurs as a response of an increase or a decrease in the heat flux driven by a change in the heating rate. Numerical simulations like 0D (e.g., Klimchuk et al. 2008; Cargill et al. 2012) and 1D hydrodynamic loop model (e.g., see Reale 2014, for a review) have attempted to model the details of plasma response as the plasma subjects to a known/unknown heating mechanism. Other simulations also tried to couple the heating and the plasma response.

In section 2.2.1 and section 3.2 we will show some results of the plasma response to the heating in a thin magnetically closed structure. Finally the radiation from the plasma can be recorded using direct imaging and/or spectral imaging of the solar atmosphere which can be studied in detail.

## 1.4 Evidence for very hot plasma in coronal loops

According to one popular scenario, coronal loops are mainly heated by short and intense energy pulses, called nanoflares (Parker 1988; Cargill 1994) formed at tangential discontinuities while magnetic tubes are twisted and braided. A strong evidence support for nanoflares might be the detection of very hot plasma ( $> 5MK$) especially in the active region.

Several authors have found evidence for the presence of very hot plasma in the active region. For instance, Reale et al. (2011) analyzed the morphology of the active region of the sun observed with SDO/AIA in three different channels namely, 94 Å, 171 Å and 335 Å channel.

By subtracting the cooler component of the hotter channel (94 Å) that is double peaked, they found that much of the plasma confined in the filamented arches that we see in 94 Å channel in the core of the active region is not warm at 1 $MK$ but it must be hot at around 6-8 $MK$.

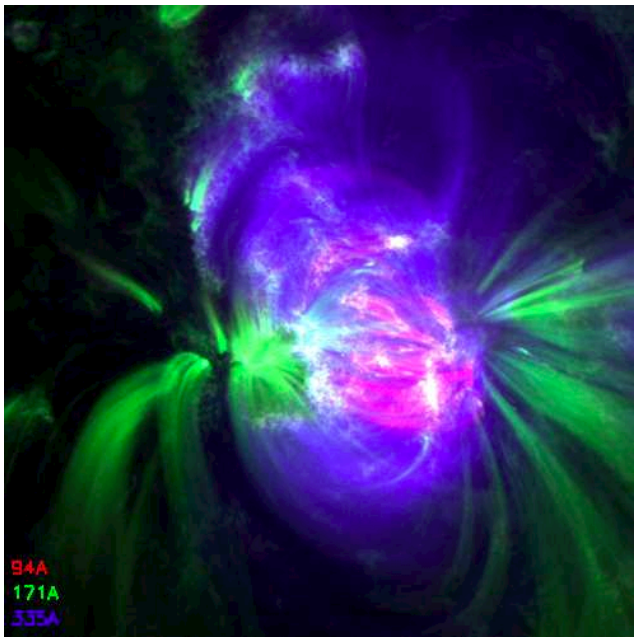


**Figure 1.4:** SDO/AIA three color full disk image combining AIA observations in the 171 Å (green), 335 Å (blue), and 94 Å (red) channels. The structures in 3 different channels are nicely complementary. The red color illustrates the very hot plasma ($> 5MK$)

Emission from very hot lines has been found in Hinode/EIS observations, and in particular from the Ca XVII at 192.858 Å, formed near a temperature of $6 \times 10^6 K$, in active region (Ko et al. 2009) and later Testa & Reale (2012) compared the morphology in a 3 color image combining the 94, 171 and 335 Å AIA spectral bands with the image obtained for Ca XVII emission from the analysis of EIS spectra. They found that in the selected active regions the Ca XVII emission is strong only in very limited areas, showing striking similarities with the features bright in the 94 Å (and 335 Å) AIA channels and weak in the 171 Å band.

Thanks to Hinode's multifilter observations, X-ray telescope provides useful information about the thermal structure of the bright X-ray corona. Temperature maps derived with combined filter ratios show fine structuring to the limit of the instrument resolution and evidence of multithermal components (Reale et al. 2007), as complemented by TRACE images. Observations including flare filters show evidence of a hot component in active regions outside of flares (Schmelz et al. 2009) and data in the medium thickness filters appear to constrain better this component of hot plasma as widespread, although minor, and peaking around $logT \sim 6.8 - 6.9$ with a tail above 10 MK (Reale et al. 2009b).

Further support comes from RHESSI data (Reale et al. 2009a; McTiernan 2009). Further evidence for minor components of hot plasma in non-flaring active regions have been found from various other instruments. Analysis in the waveband 3.3-6.1

Å and 280-330 Å with the RESIK and SPIRIT instruments, respectively, confirm the presence of a 0.1% 10 MK component at various activity levels (Sylwester et al. 2010; Shestov et al. 2010; Miceli et al. 2012).

However, while it has been proposed that AIA imaging observations of the solar corona can be used to track hot plasma(6-8 MK), it has been questioned that such emission is really at the temperature of the line sensitivity peak (Teriaca et al. 2012).

There is also some evidence that the amount of high-temperature plasma might correlate with the intensity of the active region magnetic fields because of increasing frequency of energy release (Warren et al. 2012).

Recently Petralia et al. (2014) reconstructed the emission measure (see Appendix A) distribution of several intense lines from SDO/AIA, Hinode/EIS and XRT with the aid of markov-chain Monte Carlo method. They illustrated a well-defined peak occurred at $logT \geq 6.3$ in the distribution of the hot region.

## 1.5 The multi stranded loops

The proposal of multi stranded loops has been claimed since long ago (e.g., Gomez et al. 1993). In this framework each loop is substructured into a bundle of strands each heated impulsively by a small abrupt energy release, i,e nanoflares. At the moment these strands are under-resolved and their cross section are under debate. Recently many studies have been done based on both models and analysis of observations (Beveridge et al. 2003; Cargill & Klimchuk 2004; Vekstein 2009) showing that coronal loops are multi stranded.

Among the first evidence for fine structured loops, we can point out to the work done by Di Matteo et al. (1999) . They compared the measured brightness distribution along the observed loop in NIXT to that of expected from a hydrostatic loop model, and found a low filling factor for the compact and intermediate loops ($10^{-3} - 10^{2}$) observed in NIXT suggested a fine filamentation of magnetized loops and provide a quantitative of its value.

More recent studies of address evidence for fine structuring loops observed with Hinode/EIS. For instance Tripathi et al. (2009) analyzed the active region and they showed that its related structures are more clearly defined in the lower temperature lines and appear ”fuzzy” at higher temperature as well as illustrated in the analysis of Guarrasi et al. (2010), Reale et al. (2011) by a multi stranded pulse heated loop model.

Antolin & Rouppe van der Voort (2012) presented one of the first very high resolution (100 km) spectroscopic observation of coronal rain performed with the CRisp Imaging Spectro Polarimeter (CRISP) instrument. Through estimates of the ion neutral coupling in the downflowing elongated blobs they showed that coronal rain acts as a tracer of the coronal magnetic field, therefore offered unique insights into the structures of coronal loops.

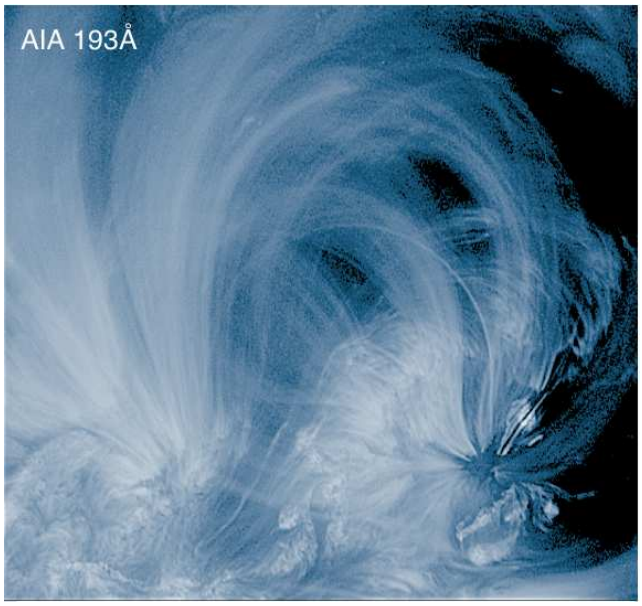


**Figure 1.5:** SDO/AIA (193 Å channel) image of finely-structured coronal loops (14 October 2011, 22:56 UT). The image was treated with a Gaussian sharpening filter with a radius of 3 pixels. Image reproduced with permission from Brooks et al. (2012), copyright by AAS.

Using the high spatial resolution imaging data (SDO/AIA) Brooks et al. (2012) demonstrated that, however in several cases loops are resolved to be monolithic structures, the majority of the loops must be composed of a number of finer un-resolved fibrils. They also constrained the number of involving fibrils needed to reproduce a particular loop structure.

In general a broad emission measure distribution indicates a multi-structure system due to the coexistence of many thermal components that are included (Cargill & Klimchuk 1997, 2004).

How the intensity scales from lower resolution imager to higher resolution one is the subject of some of the works done recently. For instance, Peter et al. (2013) found several examples where Hi-C resolves multiple linear structures in what appears to be a single loop observed with AIA. Although there were several examples where both Hi-C and AIA appear to observe the same monolithic structure i.e., the loop either had no substructure or it was below the resolving power of Hi-C. Analyzing of pixel intensities indicates the finely structure corona which was especially prevalent in the moss regions and in regions of sheared magnetic field. A relatively significant difference value between the standard deviation of those pixels intensities observed by Hi-C to that of expected from the noise indicates the presence of substructure (Winebarger et al. 2014).

## 1.6 Impulsive heating in loops

The idea of heating the corona by dissipation from current sheets (see section 1.3.1) was first suggested by Gold (1964) and later developed to form the basis of nanoflare heating modeled by Levine (1974) and Parker (1983, 1988). They claimed that dissipation of energy in such current sheets could account for the energy loss from active region. This energy loss was tabulated by Withbroe & Noyes (1977) as $\sim 10^7\, erg\, cm^2\, s^{-1}$. Parker (1988) presumes that the change in the magnetic field across the current sheet, $\Delta B$, is critical to onset. When the strength $|\Delta B|$ of the discontinuity exceeds some threshold, there is a runaway dynamical instability leading to an explosive reconnection phase. This scenario is similar to the sandpile model used to explain the comparison that is also made between results of different methods. Avalanches of magnetic reconnection (Lu & Hamilton 1991) show that the magnetic field of the corona is in a self organized critical state.

The concept of nanoflares is still under debate. Their signatures are difficult to detect through direct observation because the corona is highly conductive, washing out the signatures of heating release.

Heating by nanoflares has a long history as a possible candidate to explain the heating of the solar corona, and in particular, of the coronal loops (eg., Peres et al. 1993; Cargill 1993; Shimizu 1995; Judge et al. 1998; Mitra-Kraev & Benz 2001; Katsukawa & Tsuneta 2001; Mendoza-Briceño et al. 2002; Warren et al. 2002; Warren et al. 2003; Cargill & Klimchuk 1997, 2004; Spadaro et al. 2003; Müller et al. 2004; Testa et al. 2005; Reale et al. 2005; Taroyan et al. 2006; Vekstein 2009).

The coronal tectonics model (Priest et al. 2002) is an updated version of Parkers nanoflare theory, for which the motions of photospheric footpoints continually build up current sheets along the separatrix boundaries of the flux coming from each microscopic source (Priest 2011).

Loop models with nanoflares, and, in particular, those considering a prescribed random time distribution of the pulses deposited at the footpoints of multi-stranded loops have been able to explain several features of loop observations, for instance, of warm loops from TRACE (Warren et al. 2002; Warren et al. 2003).

The shape of the emission measure distribution is, in principle, a powerful tool to constrain the heating mechanisms. The width in temperature provides information about the temporal distribution of a discontinuous heating mechanism: for a broad (multi-thermal) distribution the simultaneous presence of many temperature components along the line of sight may be produced by many strands randomly heated for a short time and then spending most of the time in the cooling, thus crossing many different temperatures. A peaked distribution, i.e., plasma closer to an isothermal condition, indicates a plasma sustained longer at a certain temperature, with a heating much more uniform in time than for multi-thermal loops. However, the constraints on heating from emission measure distribution are largely debated; it has been found

that, although heating by single pulses might explain the majority of differential emission measures (DEM) derived in the literature (Bradshaw et al. 2012) and that trains of nanoflares might explain practically all of them (Reep et al. 2013), the uncertainties in the data analysis and DEM reconstruction are too large reach conclusive answers.

The amount of energy input to the whole corona by nanoflares is a matter of difficulty, some studies attempted to find their contribution weight in heating the corona. Hudson (1991) pointed out that the flare occurrence follows a power law distribution such as:

$$dN = E^{-\alpha} dE \tag{1.2}$$

where $dN$ is the number of events per energy interval $(E, E + dE)$ and $\alpha$ is the power law index which describes if the more weight in heating the corona is given to the flares or the scaled down version (i.e., nanoflares). Some attempts have been done to investigate this index to constrain the spatial scale of the heating events in both the active region and quiet sun using different models and different methods (Benz & Krucker 1998; Parnell & Jupp 2000; Bazarghan et al. 2008; Tajfirouze & Safari 2012). For instance, the majority of analysis to constrain this index based on counting the events in bins of average $dE$ in a series of observation deduced $\alpha \approx 1.7$ (Lin et al. 1984; Shimizu 1995; Aschwanden & Parnell 2002). Parnell (2004) demonstrated that one can obtain a ranging from 1.5 to 2.6 for the same data set using different but still reasonable sets of assumptions.

Hi-C observations of the upper TR at the footpoints of hot ($> 4MK$) coronal loops (the moss) have recently revealed rapidly variable emission, consistent with coronal nanoflares due to slipping reconnection.

However, the lack of spectral information in Hi-C data precludes an accurate determination of the plasma properties (e.g., plasma flows at different temperatures) and therefore prevents a detailed study of the physical processes at work (Testa et al. 2014).

## 1.7 Loop modeling

In typical coronal conditions the plasma $\beta$ parameter is less than unity , the temperature is a few MK and the density spans within the range $10^8 - 10^{10}\, cm^{-3}$, the magnetically confined plasma can be assumed as a compressible fluid which can transport momentum and energy along the magnetic field line (Rosner et al. 1978; Vesecky et al. 1979). The effect of the magnetic field (especially in the case of hydrodynamic loop modeling) is to constrain the plasma to move along the magnetic line topology. Under such conditions and neglecting the gradients across the field direction, effect of curvature, no uniform loop shape, magnetic twisting, currents and transverse waves we can model the evolution of the plasma confined in a single loop by one dimensional hydrodynamic equations.

Several authors have solved the hydrodynamic equations considering a steady state loop which does not undergo a striking change in either brightness or structure. Many attempts have also been done to solve the sets of conservation equations numerically (e.g., Nagai 1980; Peres et al. 1982; Doschek et al. 1982; Nagai & Emslie 1984; Fisher et al. 1985; MacNeice 1986; Gan et al. 1991; Hansteen 1993; Betta et al. 1997; Antiochos et al. 1999; Ofman & Wang 2002; Müller et al. 2003; Bradshaw & Mason 2003; Sigalotti & Mendoza-Briceño 2003; Bradshaw & Cargill 2006).

The aim and the concept of numerical loop modeling is to study the physics of the coronal loops including the response of the confined material to the external drivers and to describe the consequent evolution, and eventually to derive the predictions to compare with observations. Including a relatively thick, cool and dense chromosphere and also transition region is important for a correct description of the mass transfer driven by transient heating (e.g., Antiochos 1979; Hood & Priest 1980; Bradshaw & Cargill 2013). The boundary layer which separates the coronal portion of a loop structure from the photosphere is critical to understanding the loop dynamics; This layer will determine the loop plasma pressure and the pressure largely defines the coronal loop radiative loss; (cf., Rosner et al. 1978).

In general the initial condition of a loop is described as one in which the loop is in hydrostatic equilibrium, cool ($10^4 \sim 10^6\ K$) and tenuous ($\sim 10^8\ cm^{-3}$).

A key parameter in investigating the evolution of the loop plasma is the heating function which has a role as a driver. It has to consider both spatial and temporal profiles.

From the results of the model we can derive the observables, i.e., the emission of the plasma which is a function of both the density and temperature.

The effects of the magnetic field in hydrodynamic loop codes are implicit. MHD codes include the magnetic field explicitly and study systems with more complex geometry. Whereas most the hydrodynamic models outputs are dealing with the plasma response to a prescribed artificial heating, MHD codes treat the heating function properly as well as plasma response.

Considering the loop as a bundle of substructured strands, another approach on the loop description has been also implemented. The approach has been adopted both to describe the loop as static (Reale & Peres 2000) and as heated impulsively by nanoflares (Warren et al. 2002; Guarrasi et al. 2014).

### 1.7.1 Monolithic loops

If the coronal loops emission does not change for a duration long enough to be compared to the plasma cooling time, they can be assumed as a system in equilibrium for most of their life time.

For a coronal loop in hydrostatic equilibrium, we can apply several simplifying assumptions: symmetry with respect to the apex, constant cross section, length much

larger than the pressure scale height, heat deposits uniformly along the loop, Low thermal flux at the base of the transition region,the pressure then is uniform along the loop which is then described by an energy balance between the heat input and the two main losses (thermal conduction and radiative loss). Integrating the energy equation one can simply obtain the scaling laws of Rosner et al. (1978)

$$\begin{aligned} T_{0,6} &= 1.4(PL_9)^{\frac{1}{3}} \\ H_3 &= 3p^{\frac{7}{6}} L_9^{-\frac{5}{6}} \end{aligned} \tag{1.3}$$

where $T_{0,6}$, $L_9$, $H_{-3}$ are the loop maximum temperature $T_0$, length $L$ and heating rate $H$, measured in units of $10^6 K$, $10^9\, cm$ and $10^{-3}\, erg/cm^3 s$ respectively. Equivalent scaling laws have been also found independently by Craig et al. (1978) using analogous model in the same framework. More general scaling laws were also found by Hood & Priest (1979).

Scaling laws are extremely useful to explain observed properties. They are able to provide a basic physical reference frame to interpret any loop feature.

### 1.7.2 Structured loops

In a scenario that loops are made up of a bundle of strands, each evolving independently of the others under the effect of short, intense and discrete heat pulses, the whole loop can be globally maintained steady.

Although, the loop emission remains steady, each strand undergoes a continuous dynamic evolution. The evolution of these filaments has been studied from observations and models. (e.g., Nagai 1980; Peres et al. 1982; Cheng et al. 1983; Nagai & Emslie 1984; Fisher et al. 1985; MacNeice 1986; Betta et al. 2001).

According to Reale et al. (2007), Reale (2014) the evolution of a single coronal loop strands subject to impulsive heating is organized in four phases:

Phase I : From the beginning of the heat pulse to the temperature peak (Heating phase), in which the heat pulse is triggered in the coronal part of the loop causes the temperature to rise abruptly with a time scale given by the conductive time in a low density plasma.

Phase II : From the temperature peak to the end of the heat pulse (evaporation phase) in which the temperature remains at maximum level and the previously heated plasma expands upward and fills the strand. Depending on the place of triggering the heat pulse (loop apex or footpoint) the chromosphere will be heated by conduction (if heating is released at the loop apex) or directly (if heating occurs at the footpoint).

Phase III : From the end of the heat pulse to the density peak (conductive cooling), the plasma immediately begins to cool due to the very efficient thermal conduction

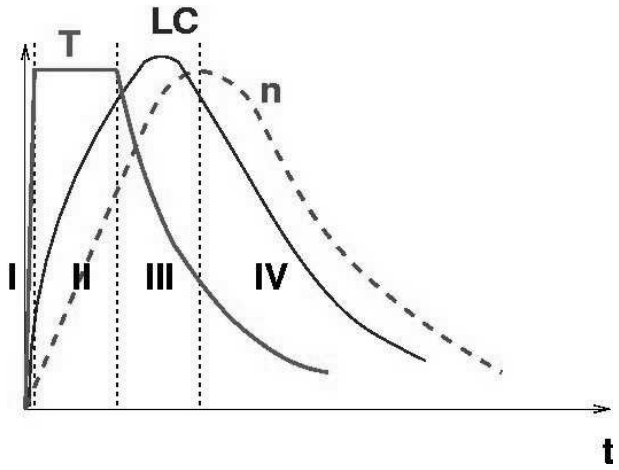


**Figure 1.6:** Scheme of the evolution of temperature (T,nthick solid line), X-ray emission, i.e., the light curve (LC, thinner solid line) and density (n, dashed line) in a loop strand ignited by a heat pulse. The strand evolution is divided into four phases (I, II, III, IV, see text for further details). Image reproduced with permission from Reale et al. (2007), copyright by ESO.

with a time scale given by:

$$\tau_c \approx 1500 \frac{n_9 L_9^2}{T_6^{\frac{5}{2}}} \tag{1.4}$$

where $n$ is the particle density $10^9\, cm^{-3}$ and at the end of the heat pulse.

Phase IV : As soon as the conductive cooling time becomes equal to radiative cooling time (radiative cooling phase), the density is at its higher level and the loop depletion starts gradually. Since the pressure decreases in this phase as a consequence of the radiative loss, the loop will no longer be able to keep its configuration balance; so draining or plasma condensation occurs as the radiation loss overcomes the thermal conduction. The time scale for radiative loss is given by:

$$\tau \approx 3000 \frac{T_{M,6}^{\frac{3}{2}}}{n_{M,9}} \tag{1.5}$$

where $T_M(T_{M,6})$ is the temperature at the time when maximum density is reached.

The evaporation phase lasts a few tens of seconds, if the impulsive heating term is active for a time significantly longer than the evaporation phase. So phase II will extends right in figure 1.6 and the thermal conduction cooling will apparently be removed. In this case, there is generally enough time for a quasi-stationary state to be reached in the corona before the heating is switched off.

The presence of phase III implies a delay between the temperature peak and the density peak. It's a signature of relatively short heat pulses whenever observed. The

shorter the heat pulse the longer the delay between the temperature peak and the density peak will be (Reale et al. 2007).

Jakimiec et al. (1992) showed that temperature and density begin to decrease simultaneously if the heating lasts enough to reach equilibrium. If the pulse ceases to heat the plasma before the loop reaches equilibrium state the so-called underdense plasma in which the density maxima is lower than the value in equilibrium (Cargill & Klimchuk 2004) occurs.

The heated plasma spends most of its life time in decay phase, therefore more attention has so far been paid to the relaxing phase. The study of the decay phase typically offers more opportunities of time resolved data analysis. Serio et al. (1991) considered a static state for the initial loop condition with spatially uniform heating and derived the thermodynamic decay (Pure cooling) of a heated confined plasma from the energetic with some simplifications. In its latest version the cooling time was updated as (Reale et al. 2007):

$$\tau \approx 500 \frac{L_9}{\sqrt{T_{0,6}}} \tag{1.6}$$

## 1.8 Time resolved analysis

The loop emission variability is not a trivial issue. The emission of coronal loops has been found to vary on various time scales. It depends strongly on the density (a fraction of the square of the density) and less on the temperature. Therefore, variations are neither direct signatures of heating episodes, nor even of the local compression (because the plasma is free to flow along the magnetic field lines). Only through the study of the whole loop evolution can one be able to explain the variations. An important issue in investigating and measuring the variations is the sensitivity of the pass bands instrument. For instance, EUV channels are typically narrow pass band filters and this will lead a high sensitivity to variations. The heating and cooling of the plasma leave signatures as turn on and off in the observation rapidly as they cross the band width sensitivity. On the other hand, X-ray telescopes have wide pass band filters, sensitive to the emission from hot plasma but not having much advantages of the temperature sensitivity as the narrow band has. The signal to noise ratio is significantly higher in this kind of filters. Separately, the spectroscopic observations have considerably high sensitivity to temperature variations, but they own normally a low cadence. Indeed they can trace variations on large time scales.

According to Reale (2014) time analysis of coronal loop observations can be mainly classified to address two main classes of phenomena:

- Temporal variability of steady structures
- Single transient events such as flare-like brightenings

Early studies of time resolved emission dealt with variability of hot x-ray loops observed by S-054 on board Skylab. The derivation of the sizes and shapes of x-ray emitting loops brightened by flares and other coronal transients, combined with estimates temperature and emission measure from the photographs led to estimates of brightness decay times for coronal loop energy loss mechanism (Krieger 1978). The observed soft x-ray brightening decay times found to be always longer than those computed from conduction cooling (Shimojo et al. 2002). Measured decay time also showed continuous evaporation of coronal plasma driven by thermal conduction from x-ray brightness (Antiochos & Sturrock 1976).

Higher temporal and spatial resolution observations of several x-ray bright points (XBPs) demonstrated intensity variability over a wide variety of time scales from a few minutes to hours as well as rapid change in their morphology (Strong et al. 1992).

Shimizu et al. (1994) classified a set of transient brightenings observed by YOHKOH soft x-ray in terms of morphology and time evolution. They clustered them into multiple loop brightenings and single structure brightenings and found that for multiple brightenings the loops tend to brighten from their footpoints.

Analyzing the plage region emission of the TRACE $FeIX/FeX$ $171\mathring{A}$ images, Berger et al. (1999) found the fine scale motions and brightness variations of the emission to occur on time scales of 1 minute or less.

Variability analysis of hot and cool loops in several UV spectral lines observed with SoHO/CDS (Di Giorgio et al. 2003) have been done as well as that of performed for TRACE warm loops (e.g., Reale et al. 2000).

The first spectroscopic evidence of plasma condensation taking place in coronal loops was found by O'Shea et al. (2007) using temporal series data from the Coronal Diagnostic Spectrometer (CDS) on board SoHO.

Several numerical simulations (Müller et al. 2004) are in good agreement with observational evidence (e.g., TRACE observation of Schrijver 2001). High cadence time series of simultaneous EIT and $H_\alpha$ data of (De Groof et al. 2004) proposed a condensation evaporation cycle for coronal loop.

Attempts to find evidence for continuous heating or frequent heating by nanoflares has also been done by taking the advantage of high temporal cadence data from Solar X-ray telescope Imager (SXI) on board Geo-Synchronous Operational Environmental satellite 12 (GOES-12). Analysis of observed light curves suggested that the durations and characteristic time scales of evolutionary phases (rise, main and decay phase) are much longer than the cooling time, indicating a slow enhancement in the loop average heating rate, reaches a maintenance level, and then decrease slowly. This suggested that a single heating mechanism operates for the entire lifetime of the loop (López Fuentes et al. 2006). Further support for continuous heating was also done by joining the YOHKOH/SXT (sensitive to the hot plasma $> 2\,MK$) and TRACE (sensitive to the cool plasma $\sim 1\,MK$) observations (Sakamoto et al. 2008), analysing the auto correlation functions to obtain the duration of the intensity fluctuations. The duration of

the intensity fluctuations for the SXT loops was found to be relatively short, while that for the TRACE loops agree well with the characteristic cooling time scale. This was also consistent with the frequent heating loops by nanoflares. The energy of nanoflares was estimated to be $10^{25}\,erg$ for SXT loops and $10^{23}\,erg$ for TRACE loops and their occurrence rate about 0.4 and 30 nanoflares per second respectively (Sakamoto et al. 2009).
More recently, light curves in individual pixels have been investigated in the X-ray band to search for significant variability connected to variable heating. Although some pulses are detected, most of the emission in active region cores and loops has been found to be steady on the timescale of hours with fluctuations on the order of $15\%$ and with no correlation between warm and hot emission (Warren et al. 2010a, 2011). Improving on previous studies (Sakamoto et al. 2008), high cadence observations with the Hinode/XRT have revealed that the distributions of intensity fluctuations have small but significant and systematic asymmetries. Part of this asymmetry has been explained through a tendency for exponentially decreasing intensity, i.e., the plasma has been cooling for most of the time (Terzo et al. 2011).
Loop light curves have been systematically analysed also in the EUV band. A systematic tendency has been found to have ordered time lags from channels sensitive to emission from hotter plasma to cooler plasma, that is also evidence for dominant cooling (Viall & Klimchuk 2011, 2012). Light curves in the EUV band have been analysed also with a different approach: they have been compared to simulated ones obtained from sequences of random pulses with power-law distribution (Tajfirouze & Safari 2012). Artificial neural network (ANN) was used for the comparison and it was found many that light curves are matched by those generated from events power-laws with a steep index ($> 2$). While studying the long-term evolution of active regions on the large scale, it was found that active regions show less and less variability as they age (Ugarte-Urra & Warren 2011), thus suggesting a qualitative change of heating frequency with time. At the other extreme of the smallest scales, the Hi-C observations show in some moss regions variability on timescales down to 15 s, that may indicate the presence of heating pulses of comparable duration.

## 1.9 Scope of this work

Finely stranded corona, which may be heated impulsively by small scale abrupt energy release, the so-called Nanoflares, may explain the high temperature corona (Reale et al. 2011; Viall & Klimchuk 2012). These pulses might heat the plasma temporarily to temperatures well above the average coronal temperature, and therefore this scenario is supported by the evidence for small amounts of ultra-hot ($> 5\,MK$) plasma (McTiernan 2009; Reale et al. 2009a,b; Testa et al. 2011; Miceli et al. 2012; Testa & Reale 2012; Brosius et al. 2014; Petralia et al. 2014; Caspi et al. 2015).

Investigating the weight by which Nanoflares and small scale events are dominant is challenging ( 1.6).

Extrapolating from the distribution of larger events (flares) to the scaled down version (micro and Nanoflares) shows that for a power law index which is greater than the critical value (2) the small scale events are dominant in heating the corona. Here we focus on the building blocks of the confined solar corona, the bright curved magnetic flux tubes called coronal loops.

According to several recent works (Klimchuk et al. 2008; Cargill et al. 2012; Viall & Klimchuk 2012) the heating pulse are released at spatial scales that are smaller than the cross section of a coronal loop. Each loop must then be sub-structured into bundle of thin strands that evolves independently of the others. Since the strands are unresolved at the moment, the cross-section of the smallest components is under debate. On the other hand, the very efficient thermal conduction along the magnetic field lines at coronal temperatures inhibits also the measurement of the duration of the individual heat pulse.

This work extends the analysis of an active region that has shown evidence of small amounts of very hot plasma (Reale et al. 2009a, 2011; Testa & Reale 2012). This area is appropriate to search for signatures of small scale heat pulses.

This work will mainly be splitted into two parts: temproal resolved analysis and spatially resolved analysis of bright pixels of EUV emission.

In the first part we are in reality investigating the emission variability at the smallest possible scale and look for signatures of heating and possibly elementary heating events. We model the Extreme Ultraviolet emission observed by the Solar Dynamic Observatory (SDO) from the active region core using a hydrodynamic model of bundles of strands heated by a storm of nanoflares with the aid of a 0D hydrodynamic loop model. In the active region core we extract the light curves of both a sample single pixel and a row of neighboring pixels in different channel bands. We generate model light curves by summing over random events (with different energy) and we compare them to observed ones using two independent methods: an artificial intelligent system based on a Probabilistic Neural Network (PNN) and a simple cross-correlation technique. The simultaneous comparison of the light curves in different channels allows us to address the multi-temperature structure of the loop that is a key point when we consider such a structured heating.

We improve this work in the second part by including spatially resolved analysis to know that how the temporal evolution of the magnetically confined plasma changes in different position along the loop. In order to do that we switch from 0D hydrodynamic loop model to 1D hydrodynamic loop model that can resolve the loop spatially.

Some more detailed issues about the active region coronal loop will be consequently investigated. This other analysis will lead us to find new diagnostical tools to have information about coronal heating from imaging data.

This work has been the subject of two papers:

- " Time-resolved emission from bright hot pixels of an active region observed in the EUV band with SDO/AIA and multi-stranded loop modeling " by:

  E. Tajfirouze, F.Reale, A. Petralia, P. Testa
  Accepted for publication in the Astrophysical Journal

- " EUV flickering of coronal loops: A new diagnostic of coronal heating " by:

  E. Tajfirouze, F.Reale, G. Peres, P. Testa
  Submitted to the Astrophysical Journal Letter

# Chapter 2

# Time Resolved Analysis and modeling an active region

This work extends the analysis of an active region that has shown evidence of small amounts of very hot plasma ($> 5$ MK) in most of the region core and out of proper flares (Reale et al. 2009a, Reale et al. 2011, Testa et al. 2012). This area is appropriate to search for signatures of small scale heat pulses.

## 2.1 Observation

### 2.1.1 Solar Dynamic Observatory

The Solar Dynamics Observatory (SDO) is a NASA mission Launched on February 11, 2010.

SDO consists of a suite of instruments: the Extreme Ultraviolet Variability Experiment (EVE) which measures fluctuations in the Suns ultraviolet output, the Helioseismic and Magnetic Imager (HMI) which maps magnetic and velocity fields at the surface of the Sun and the Atmospheric Imaging Assembly (AIA) which is used in our analysis and is described briefly in the following.

AIA provides multiple simultaneous high resolution full disk images of the corona and transition region up to 0.5 solar radius above the solar limb with 1.5 arcsec spatial resolution and 12 second temporal resolution. The AIA consists of four telescopes that employ normal incidence, multilayer-coated optics to provide narrow band imaging of seven extreme ultraviolet (EUV) band passes centered on specific lines: Fe XVIII (94 Å), Fe VIII,XXI (131 Å), Fe IX (171 Å), Fe XII,XXIV (193 Å), Fe XIV (211 Å), He II (304 Å), and Fe XVI (335 Å). One telescope observes C IV (near 1600 ) and the nearby continuum (1700 Å) and has a filter that observes in the visible to enable coalignment with images from other telescopes. The temperature diagnostics of the EUV emissions cover the range from $6 \times 10^4 K$ to $2 \times 10^7 K$.

### 2.1.2 Data analysis

We analyze SDO/AIA observations of AR11117 on 2010 October 28, from 2:00 UT. We consider a 500 $\times$ 500 pixel region in three channels: 94 Å, 171 Å, 335 Å. The narrow passbands of the AIA channels contain bright spectral lines emitted by plasma at different temperatures. In particular, we initially choose the observations in three EUV channels, namely the 94 Å, 171 Å and 335 Å that are most sensitive to the emission of plasma in a broad range of temperatures, i.e. at 6 MK, 1 MK and 3 MK respectively. The response function in the 94 Å channel is double peaked, with a cooler peak below 1MK (Boerner et al. 2012, Boerner et al. 2014, Testa & Reale 2012) . However, in active region cores the hotter peak is generally dominant (e.g., Testa et al. 2012).

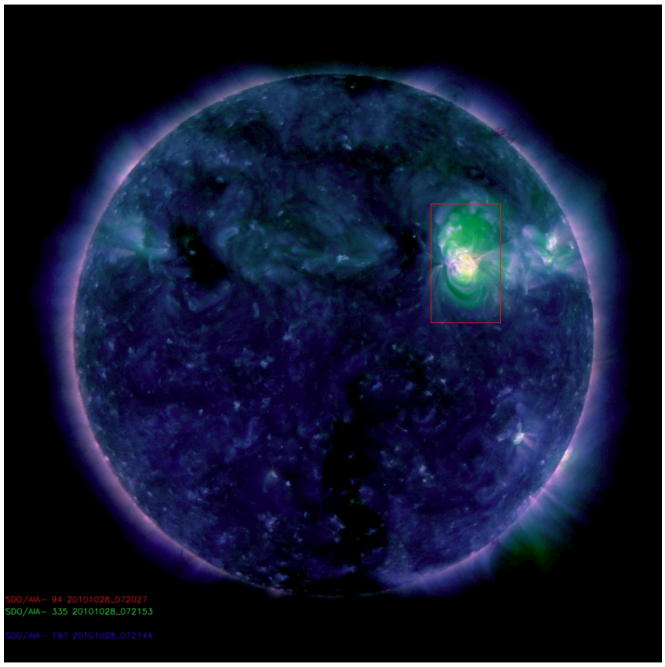


**Figure 2.1:** Full Disc image of the sun Observed by SDO on 28 october 2010. The red box shows the selected region to analyse.

We use level-1.0 data, after standard processing of level-0 data (bad-pixel removal, despiking, flat fielding). Data are obtained from a standard observing series with cadence of 12 s in all channels, and exposure times of 2 s in the 171 Å channel and 2.9 s in the 335 Å and 94 Å channels. The channels have very different sensitivity to the solar coronal emission (see., Reale et al. 2011), resulting in different signal-to-noise ratios. Figure 2.2 shows the internal part of the active region in the 94 Å, 335 Å, and 171 Å channels.

In the 335 Å channel, the active region core is covered quite uniformly by a large

number of bright arches. In the southern part (20 arcsec $\leq$ Y $\leq$ 55 arcsec), the arches coalesce to form a uniform bright band. In the northern part, we can identify three brighter loop groups in a background of more diffuse emission. A few very bright spots are visible at the center of the region. Overall the region has quite a diffuse appearance and individual loops cannot be clearly resolved.

In the 94 Å channel, overall we see a very similar morphology and many bright structures are clearly cospatial with those observed in the 335 Å channel. The most striking difference from the image in the other channel is in the core itself: in the southern part, while in 335 Å the arches are densely packed and uniform, in 94 Å they have greater contrast, i.e., we see an alternation of bright and fainter structures. In the northern part, we are even able to resolve very thin bright east-to-west bridges, in the same location where thicker arches are present in the softer channel. Overall, in the 94 Å channel, the loop systems appear sharper, the observed emission largely less fuzzy, and we can resolve thinner bright structures than in the 335 Å channel. This is exactly the effect expected by Reale et al. (2011), and predicted by Guarrasi et al. (2010).

In the 171 Å channel, the active region shows quite a different morphology. Many structures are complementary to those observed in the other channels (Reale et al. 2007). The core appears depleted of arch-like structures. Only a few of them are visible, and they look quite different from those in both the other channels. The arch-like structures are instead replaced by bright moss. This moss is a well-known feature of this soft channel, already studied in Normal Incidence X-ray Telescope (NIXT) and Transition Region and Coronal Explorer (TRACE) observations and commonly explained as the bright warm footpoints of (hot) high-pressure loops (Peres et al. 1994; Fletcher & de Pontieu 1999; Martens et al. 2000).

For our study we need the highest possible space and time resolution to try to capture the small temporal and spatial scales expected for nano-flare heating. Therefore, we consider the smallest scale pixel region, i.e. single pixels, and the full time resolution. Figure 2.2 shows the active region core in the 3 AIA channels and the location of the pixels where we have extracted light curves. We skipped the 171 Å channel for further analysis, because it is affected severely by underlying moss emission.

By definition, this emission is not included in our modeling, which comprises only the coronal part of the loops. Since this emission is out of the scope of our work, from now on we will address only the comparison with the 94 Å and 335 Å channels, which instead are sensitive to the body of the coronal loops. We have ascertained that the low temperature contribution to the 94 Å channel is negligible (by rescaling the emission in the 171 Å channel, e.g., Reale et al. 2011).

We consider 246 and 228 successive images in the two respective channels, corresponding to timeseries of total duration of $\sim$ 1 hour, i.e., much longer than typical loop plasma cooling times (Reale 2014). We carefully aligned images between the two different channels via cross correlation using the align_cube_correl procedure in Solar SoftWare (SSW) package. The time distance between the images is typically 12 sec-

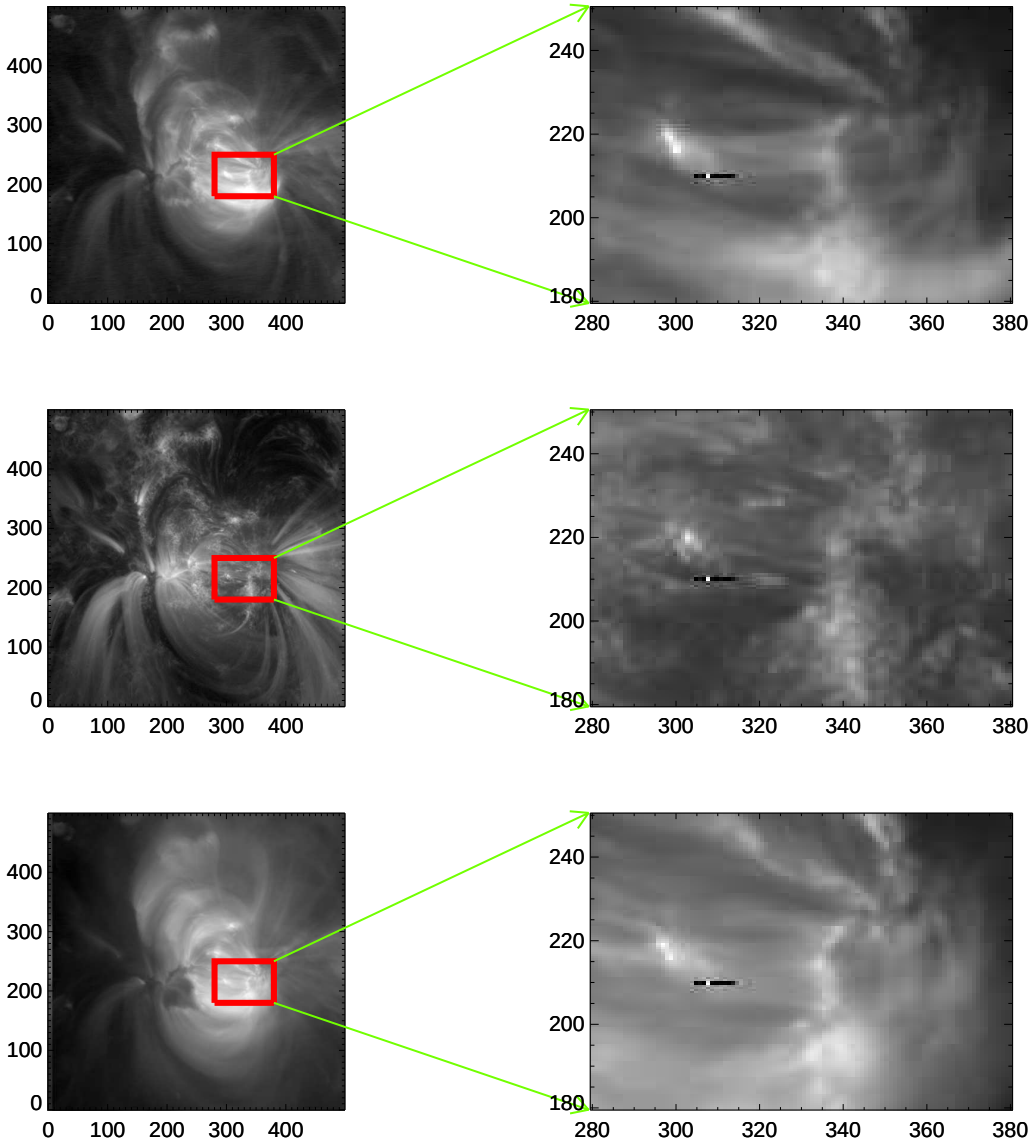


**Figure 2.2:** Left column: from up to down is the images of the active region in the 94 Å, 171 Å and 335 Å channels respectively. Right column: zoomed view of the insets in the left images. The single pixel (white) and row of pixels (black) for analysis are marked.

onds, but there are some gaps up to $\sim$ 1 minute. We select a single pixel in the bright and filamented core observed in the 94 Å channel, where there is evidence of very hot plasma (Reale et al. 2011). It is one where the light curve does not show prominent single-time spikes, which typically affect other pixels. We have also tried to improve for signal-to-noise ratio. Our choice has been to sum the emission in a few nearby pixels. The orientation of observation frame vs the active region shows that many structures are practically aligned in a left-right direction. Actually, we have identified a few rows of pixels where the emission shows a coherent time behaviour, i.e. they

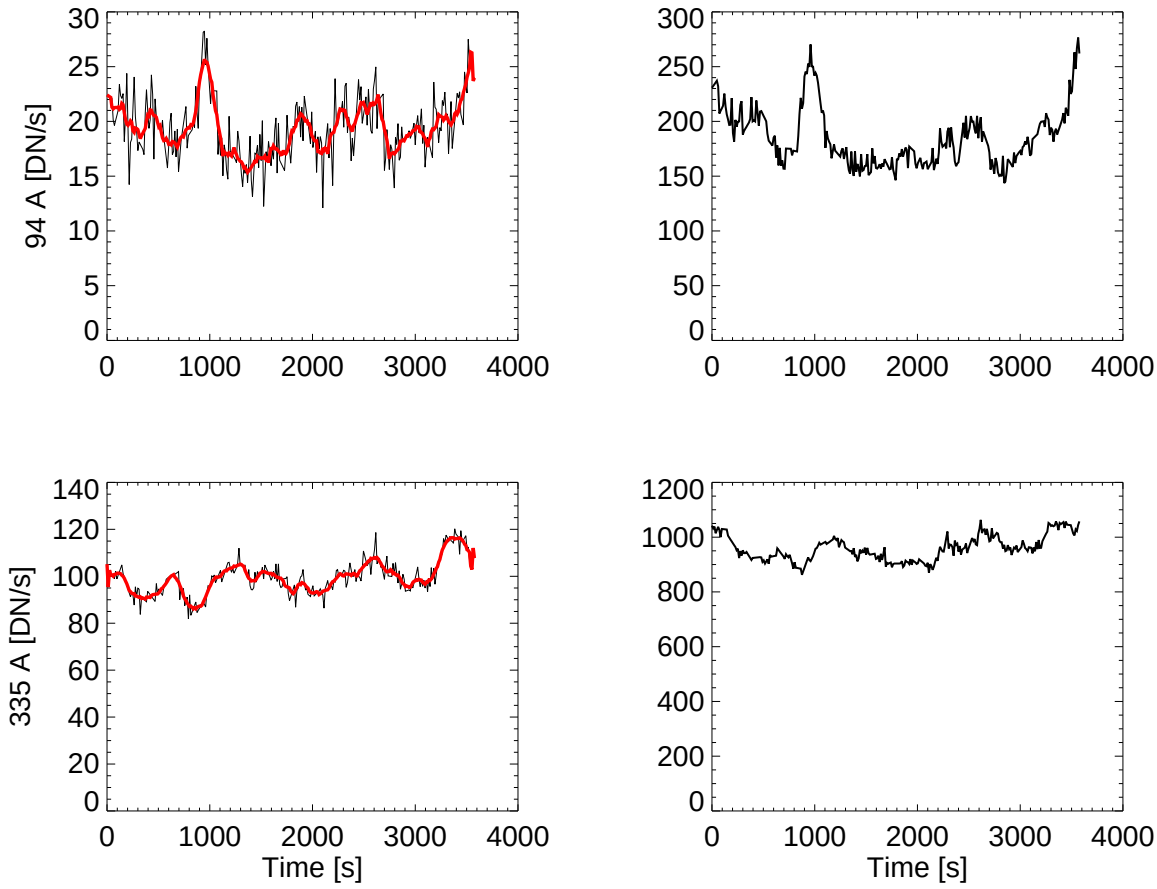


**Figure 2.3:** Light curves in two AIA channels (up to down: 94 Å and 335 Å) from the single pixel (left column) and the row of pixels (right column) indicated in figure 2.2. Smoothed light curves of the single pixel are also shown (red).

probably intercept the same loop strands where the confined plasma evolves coherently. We select a row of 9 pixels which includes the single pixel. Figure 2.3 shows the light curves for the single pixel and for the row of 9 pixels. To better show the trends and features of the single pixel emission we also show the light curves smoothed with a boxcar of 8 data points. The single pixel allows for the maximum possible sensitivity to emission variations, but is affected by significant noise from limited photon statistics. The row of pixels reduces the photon noise but also the sensitivity to variations. The light curves show different amplitude of fluctuations in the two channels. The evolution in the 335 Å channel is rather smooth, with an overall variation range of $\sim 30\%$. In the 94 Å channel we see larger fluctuations and even a localised peak $\sim 50\%$ above the average with a duration of $\sim 5\,min$. The bump shows equal rise and decay times. We find similar trends and features and similar results of our analysis also for other pixels.

From the observation we estimate that the loops inside the active region core have

a length of $\approx 5 \times 10^9\, cm$ and we will assume this as our reference loop length from now on.

## 2.2 Model

Multi-stranded pulse-heated loop models have been recently successful in explaining the presence of hot plasma in the active region. In the following we use 0D loop model (Klimchuk et al. 2008, Cargill et al. 2012) to study the emission in EUV.

In our scenario a single pixel of an image intercepts bundles of strands along the line of sight. Then, we simulate the emission from a pixel by summing the intensities of many strands, each heated at a random time by a random energy pulse (according to a power law energy distribution).

### 2.2.1 The loop model

Our aim is to analyse the time variation of the loop emission. In the reasonable assumption that the plasma evolution does not change much from one position to the other inside a single strand that composes the loop, we focus on the description of the strand population, of the parameters of the related storm of nano-flares, and of how they combine to produce the total observed emission. In this scenario, the coronal average quantities in each strand provide enough information to describe the strand properties, but we need a good description of their time evolution.

To this purpose, we use EBTEL (Enthalpy Based Thermal Evolution of Loops), a zero dimensional time-dependent hydrodynamic model (Klimchuk et al. 2008, Cargill et al. 2012). The model has no spatial resolution, and describes the evolution of the average physical properties of the plasma confined in a single coronal flux tube. The model assumes that the loop is symmetric with respect to the apex, and therefore describes half of it. A physical key concept in the model is the enthalpy which has the main role in transferring energy budget into and out of the corona. The enthalpy will certainly not produce or eliminate energy. Variations in heating rate will affect transferring of mass between chromosphere and corona. Any changes in heating rate will cause an increase or decrease in the heat flux and any excess or deficit in downward heat flux related to the transition region radiation loss will consequently derive an up flow enthalpy flux or will be compensated by a downward enthalpy flow respectively. The energy equation is:

$$\frac{\partial E}{\partial t} = \frac{\partial (Ev)}{\partial s} - \frac{\partial (Pv)}{\partial s} - \frac{\partial F}{\partial s} + Q - n^2 \Lambda(T) + \rho g_{\parallel} \tag{2.1}$$

in which

$$E = \frac{3}{2} P + \frac{1}{2} \rho v^2 \tag{2.2}$$

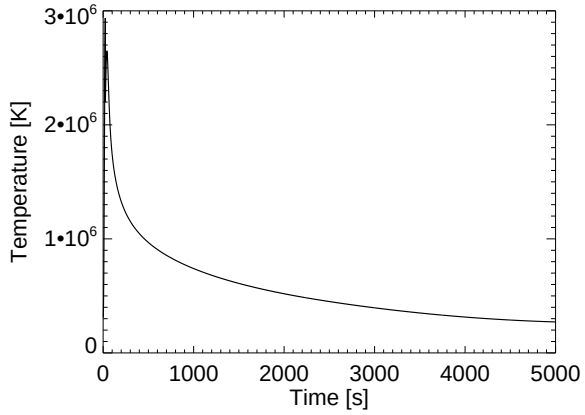


(a)

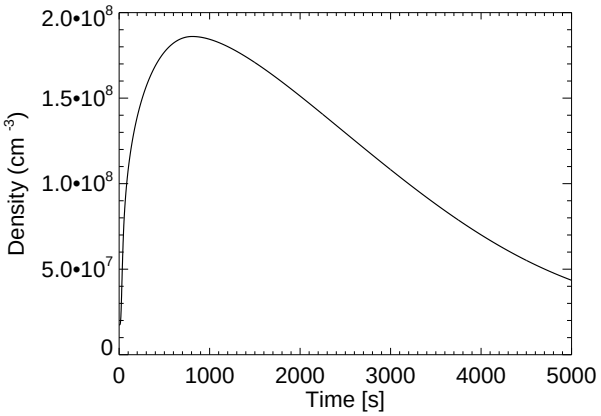


(b)

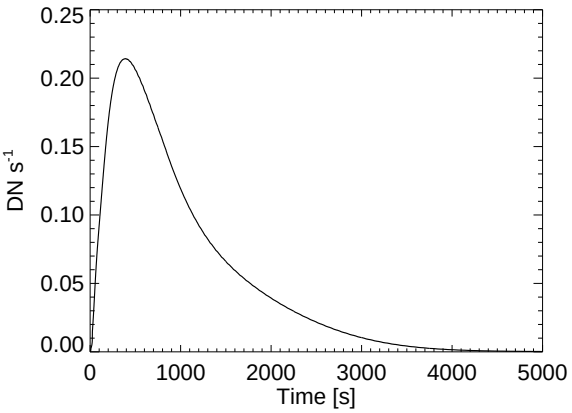


(c)

**Figure 2.4:** Time evolution of (a) temperature, (b) density and (c) AIA 94 Å intensity of a single strand, heated by a pulse of 0.003 erg $cm^{-3}$ $s^{-1}$, and 50 s duration.

E is the combination of thermal energy and kinetic energy, P is pressure, v is the bulk velocity, F is the heat flux, Q is the volumetric heating rate, n is the electron density, $\Lambda$ is the radiation loss function and $g_{\|}$ is the gravity component which is along the magnetic field. We assume classical conductivity, but we have ascertained that saturated conductivity does not change the results (and in particular the light curves, see section 2.4) significantly on the relatively long time scales of our modeling. The evolution for density and pressure can be described fully versus the coronal parameters as we integrate the energy equation over the coronal part of the loop once and separately over the transition part.

$$\frac{1}{\gamma-1}\frac{d\bar{P}}{dt} = \bar{Q} - \frac{1}{L}(R_c + R_{tr}) \tag{2.3}$$

$$\frac{1}{\gamma-1}\frac{d\bar{n}}{dt} = \frac{n_0 v_0}{L} = -\frac{\gamma-1}{2KT_0 L\gamma}(F_0 + R_{tr}) \tag{2.4}$$

where $\bar{\text{P}}$ and $\bar{\text{n}}$ are the averages of pressure and density, $R_c$ and $R_{tr}$ are the radiation losses in corona and transition region respectively, F is the heat flux, v is the bulk velocity and 0 indexes describe the values in the base of the corona. This set will be completed if we insert an equation of state.

$$\frac{1}{\bar{T}}\frac{d\bar{T}}{dt} = \frac{1}{\bar{P}}\frac{d\bar{P}}{dt} - \frac{1}{\bar{n}}\frac{d\bar{n}}{dt} \tag{2.5}$$

We use EBTEL to model the evolution of the plasma confined in single loop strands under the effect of short heat pulses. Figure 2.4 shows the evolution of average coronal temperature and density inside a single strand subject to impulsive heating. The strand is initially cool and tenuous, with a temperature of 0.24 MK and a density of $\sim 10^7$ cm$^{-3}$. A very small amount of heating ($10^{-6}\ erg\,cm^{-3}\,s^{-1}$) is constantly provided to keep the strand in equilibrium. In addition to this, we impose a heat pulse of triangular time profile having a duration of $\tau = 50\,s$ and an intensity peak of $h = 0.003\ erg\,cm^{-3}\,s^{-1}$. This heating rate corresponds to a temperature of $\sim 2.5$ MK at the equilibrium according to the scaling laws of Rosner et al. 1978. The thermodynamic decay time according to Serio et al. 1991 and Reale 2014 is $\tau \sim 800\,s$. We follow the evolution over $10^4\,s$ , i.e. more than 10 decay times in this case.

In figure 2.4 the temperature rises abruptly to $\sim 3$ MK as a consequence of the intense nanoflare. The strong heat flux drives massive evaporation from the chromosphere to the corona and the strand begins to fill with plasma to a maximum density of $\sim 2\times10^8\,cm^{-3}$. This is much lower than the equilibrium density of $\sim 3\times10^9\,cm^{-3}$, because of the short duration of the heat pulse. The temperature declines as the nanoflare shuts off by the effect of both the radiation and plasma thermal conduction toward the cool chromosphere. The density peaks later (by $\sim 10$ min) than the temperature because the evaporation continues for some time (Reale 2014). The strands

finally enter a long phase of draining as the radiation loss - the cooling mechanism- overcomes gradually the thermal conduction (Cargill et al. 2012). The density decay is quite slower than the temperature decay.

From EBTEL results we can derive the emission in the EUV. Figure 2.4c shows the light curve in the SDO/AIA 94 Å channel. The light curve has a shape in between the evolution of the temperature and of the density, because the emission is a function of both of them. So, the peak of the emission occurs $\sim 5$ min later than that of the temperature. This is a light curve of a single strand. When we look at the light curve of a pixel, we are summing the light curves of many strands that are intercepted along the line of sight in that pixel.

A single pixel may contain tens to several hundreds of strands each heated impulsively. We assume that the distribution of the heat pulses is described by a power law (e.g., Hudson 1991):

$$dN = E^{-\alpha} dE \tag{2.6}$$

where $dN$ is the number of events per energy interval $(E, E + dE)$ and $\alpha$ is the power law index. Each strand is ignited independently of the others, therefore at random times and at random intensities, according to the power law frequency distribution. Since we are unable to constrain the times and intensities, our approach is to generate a large number of different realizations of the same light curve that consists of overlapping light curves of a given number of strands. Each light curve is related to a random pulse extracted from the power law distribution and has a random start time. We generate groups of realizations, one for a given power law index, pulse duration and number of strands.

As mentioned in Section 2.1, the total loop length is fixed to $5 \times 10^9\, cm$. We choose two possible values of the power law index, i.e. $\alpha = 1.5$ and $\alpha = 2.5$. We choose either of two possible pulse durations, i.e. a short ($\tau = 50$ s) one and a long ($\tau = 500$ s) one, with respect to typical plasma cooling times. The other key parameter is the number of strands that are heated along the line of sight, and in particular we consider three possible values, N=10, 100 and 1000. We assume that each strand is heated only once during our total time lapse. In this view, the number of strands is also the number of heat pulses. There is discussion about the frequency of the heat pulses inside a single strand, whether the repetition time is large (low frequency) or small (high frequency) with respect to the typical cooling times (Klimchuk 2015). Our scenario is basically low frequency. However, we address only the high temperature emission, and similar results might be obtained with more frequent pulses, with a delay not much longer than 1000 s (see Fig.2.4c). This might be in agreement with recent constraints (e.g., Cargill 2014; Cargill et al. 2015).

We tune the range and height of the power law distributions so as to produce a bundle of strands that has the average temperature of the observed active region loops, i.e. about 3 MK. Figure 2.5 shows the energy rate distributions of the pulses obtained for

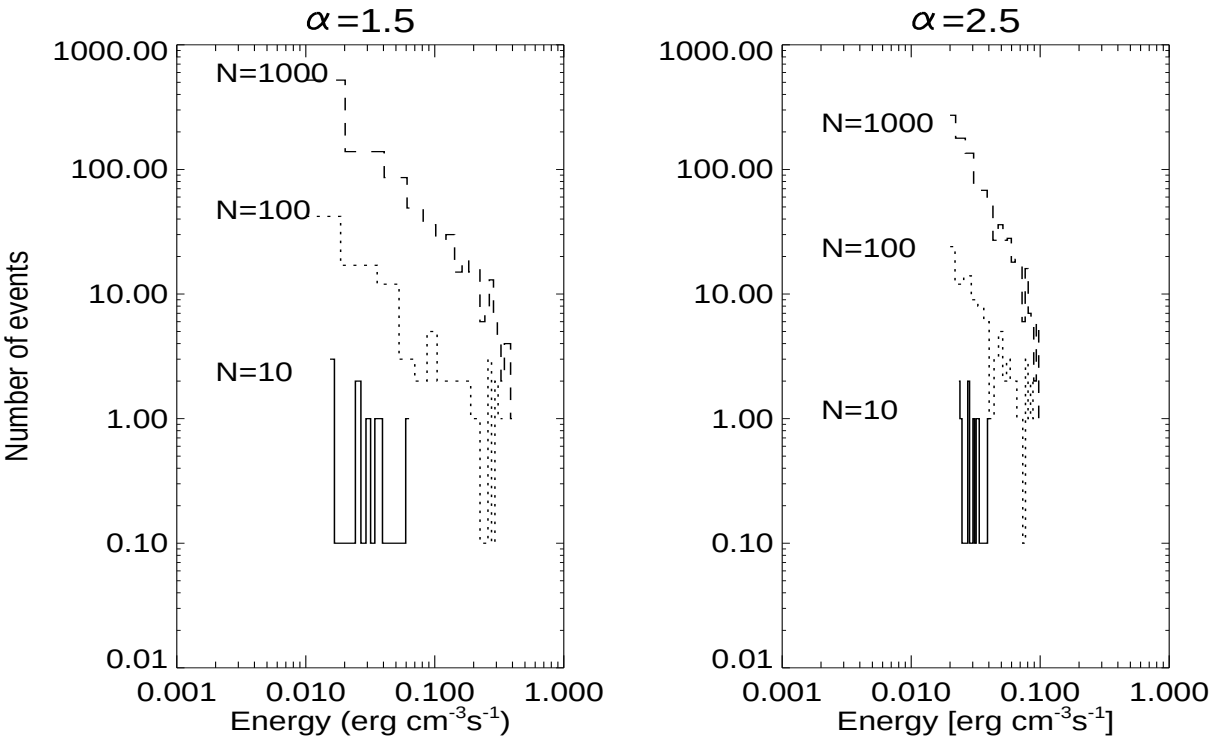


**Figure 2.5:** Left to right: The distribution of simulated energies for power law index $\alpha = 1.5$, $\alpha = 2.5$. For both the cases the duration of the heat pulses is $\tau = 50\,s$.

different numbers of strands and for the shorter pulse durations. Instead of producing one model for each energy rate, i.e. for each realisation, we have preferred to generate a grid of EBTEL models, choosing the parameters so as to span reasonably all possible loop conditions in the energy range. We then use a binary search to find the closest value of each energy from the original power law distribution to the one in the grid.

For each of the 12 combinations of $\alpha$, $\tau$, and $N$, a package of 10000 pairs of light curves (two for each realization) is produced. An example of a single realization among a specified set of parameter ($\alpha = 2.5\ \tau = 50\ n = 100$) is shown in figure 2.6.

We compare each pair of light curves to the observed ones and choose the best matching ones with the methods described in the following.

## 2.3 Methods

### 2.3.1 Probabilistic Neural Network [PNN]

Artificial neural networks (ANN) are parallel computing devices consisting of many interconnected simple processors. They share many characteristics of real biological neural networks such as the human brain. Knowledge is acquired by the network from its environment through a learning process, and this knowledge is stored in the connec-

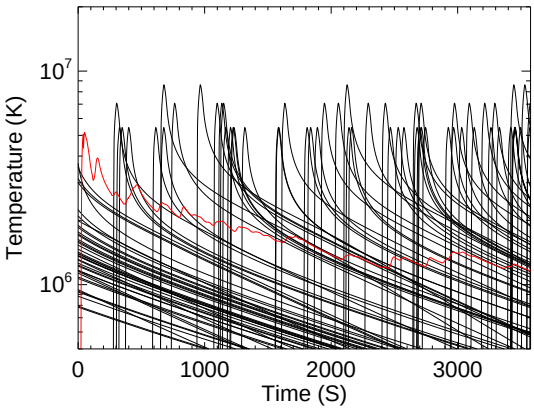


(a)

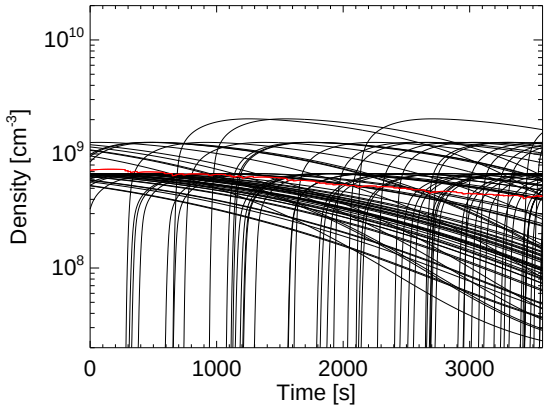


(b)

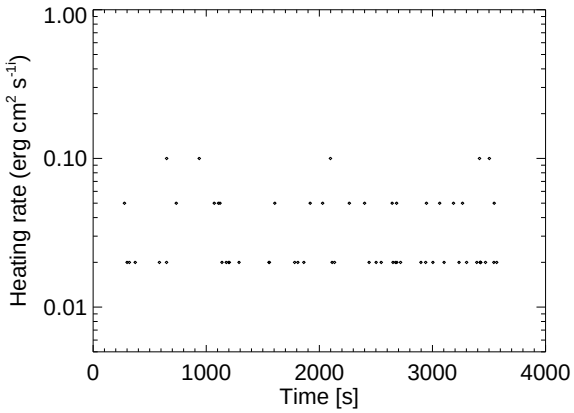


(c)

**Figure 2.6:** Time evolution of (a) temperature, (b) density and the destribution of the (c) heating rate of contributed strands, for a single realization labeled with $\alpha = 2.5$ $\tau = 50$ $n = 100$.

tions strengths (weights) between processing units (neurons). In recent years, neural computing has emerged as a practical technology with applications in many fields. The majority of these applications are concerned with problems in pattern recognition, for example, in automatic quality control, optimization and feedback control.

In the following we outline the basics and concepts of the Artificial Neural network and its purposes. We will initially make a brief review on the training algorithm which is used in the simplest and fundamental kind of artificial neural network (perceptron) which is suitable in comprehending the basics. After that we will move on to present one of the most useful kind of the neural network called Probabilistic Neural Network [PNN].

**Human and machine**

The main difference between the computer and the human mind is their structures.

Computers has been designed in such a way that they do one operation after another with a great speed. But the brain acts in a lower speed, having a great number of processors. Computers are quick and nimble but act in a serial way. On the other hand the human brain has an intense parallel structure.

Operations like watching/seeing, listening, are just parallel actions in which the very opposite and different numerous data causes different effects and different reminds in mind individually. Through comparing and combining these various data properly can the brain perform such marvelous operation.

Instead of employing one quick calculative processor to operate, the brain employees numerous unit processors called neurons to process one individual operation. Basically a great number of small (though slow compared to the computer one) processors treat one special job, collectively at the same time. The contribution of each neuron cannot be significantly important on its own. It means that if an individual neuron does not perform its duty properly, it will not affect the final output. On the contrary, computers are seriously sensitive to the errors. They have not the ability to neglect the errors, because they are not able to distribute the jobs.

One of the most important features of the brain may be its ability to learn. The brain can actually train itself (self-learning). But computers obey a pre-written program they are forced to follow step by step.

In modeling the main systems of brain, Artificial intelligence specialists investigate ways that reflect the parallel structure of the brain. These models must be able to set the knowledge (data/information) in a parallel form and process it in a parallel way.

The main purpose of the neural network calculations is to produce such machines that model the main features of the brain and the ways of its operation.

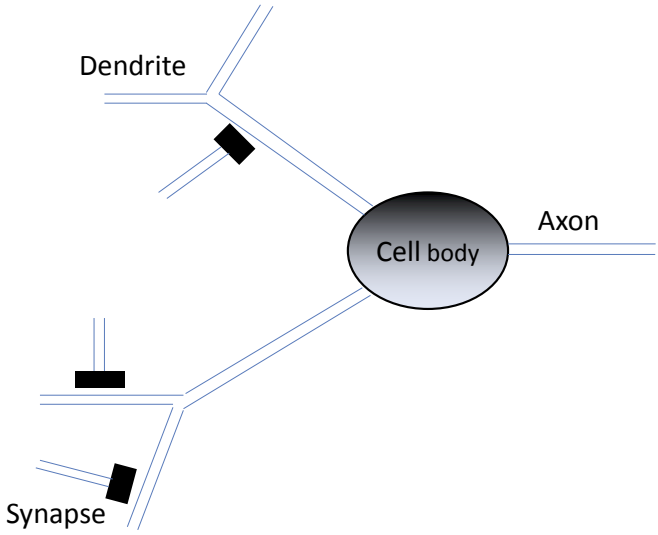


**Figure 2.7:** The main charactristics of a biological neuron: Dendrites are the input channels, axons are the ouput channels that are connected to the dendrites of the other cells, and synapses are the connection cites between the dendrites and the axons.

### Neuron modeling

The aim of modeling is to produce a more simple system which keeps the main behavior of the system and makes it easier to understand. The main role of a biological neuron is to add its input so that it exceeds a threshold value and then fire an ouput. The inputs of a neuron is fed through dendrites which are connected to the other neurons outputs by the synapses (figure 2.7). By definition the synapse change the efficiency of the input signals. The above description leads us to model a neuron:

- The output of a neuron is active [1] or non-active [0].
- The outputs only depend on the total integration of the inputs that should exceed a pre-defined threshold to activate the neuron.

The efficiency of the synapses in transferring the input signals into the cell body is modeled by a modulus which is multiplied by the neurons input:

$$\sum_{i=1}^{n} W_i X_i = W_1 X_1 + W_2 X_2 + ... + W_n X_n \tag{2.7}$$

where $X_i$ is the i'th input and $W_i$ is the weight related to the i'th connection line.

The total summation should be compared to the threshold. If it exceeds the threshold the output of the neuron is 1 and if it does not then the output will be 0 (figure 2.8). For simplicity, we can initially reduce the threshold from the total weight summation and then compare the total input with zero.

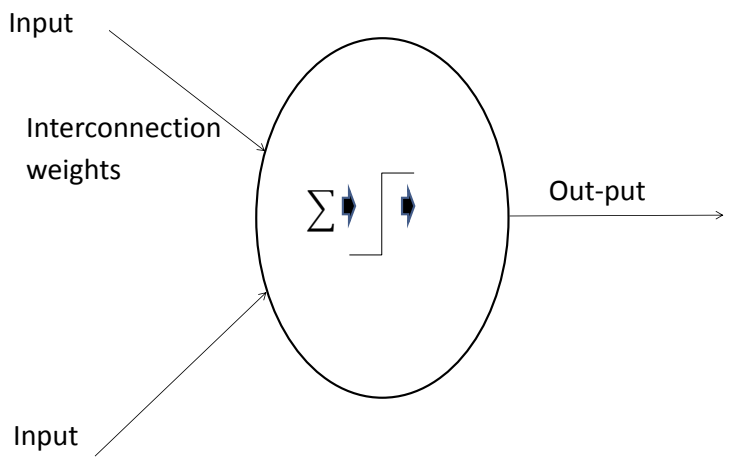


**Figure 2.8:** The main scheme of the modeled neuron. The cell body adds the inputs. If the summation exceeds the threshold then the neuron fires an output.

### Learning in symple neurons

The general guidance is to allow the neuron learn from its mistakes. If the output of the neuron is not true we let the neuron reduce the probability of making mistakes in the next performance of its operation. And if the ouput is true we make no change.

### Perceptron learning algorithm

- Determine the weights and threshold
  consider $W_i(t),\ (0 \leq i \leq n)$ as the i'th interconnection $W_i$ to be equal to -$\theta$ and $X_0$ (the first input) to be always 1. Set $W_i(0)$ to be equal to small random values. In this way we set all the weights and thresolds.

- Present the favorite input ($X_i$) and output ($\sigma(t)$)

- Calculate the real output
  $W_i(t+1) = W_i(t)$ if the output is true
  $W_i(t+1) = W_i(t) + X_i(t)$ if the real ouput is 0 and the favorite is 1 (class A)
  $W_i(t+1) = W_i(t) - X_i(t)$ if the real output is 1 and the favorite is 0 (class B)

We note that as the model response is true the weights need not to be changed. However the interconnection weights which are not efficient in putting out a wrong answer is not changed, Because their interconnection weights will be added by the input values (that are zero). Therefore it remains unchanged. The perceptron algorithm warrantee the reduction of errors in each step of training (Haykin 1999). In other words

the weights are modified step by step in such a way that the error reduces in each step of training. Some useful variations have also been introduced to the basic algorithm. The first one is to insert a coefficient smaller than 1 . It causes the interconnection weight to change slightly (and with less speed). So, the network approach the favorite answer in smaller steps. This modification changes the forth step of the algorithm as follows:

- modify the interconnection weight
  $W_i(t+1) = W_i(t)$ if the out put is true
  $W_i(t+1) = W_i(t) + \eta X_i(t)$ if the real ouput is 0 and the favorite is 1 (class A).
  $W_i(t+1) = W_i(t) - \eta X_i(t)$ if the real output is 1 and the favorite is 0 (class B).

A similar algorithm was proposed by Widrow & Hoff (1960). They suggested that it is better to change the weight more and more as the difference between the real ouput and the favorite output is high and also change it less as the real output becomes more closed to the favorite one. The rule they presented named Widrow and Hoff delta rule. They introduced the error parameter($\Delta$) and suggested modifying the weights with respect to the following algorithm:
$\Delta = d(t) - y(t)$
where $d(t)$ is the favorite output and $y(t)$ is the real ouput. So the forth step changed as follow:

- modify the weights (Widro-Hoff Delta rule)
  $\Delta = d(t) - y(t)$
  $W_i(t+1) = W_i(t) - \eta \Delta X_i(t)$

If the input belongs to class A then $d(t) = 1$ and if the input belongs to class B then $d(t) = 0$.

The above one was the basics of training algorithm used in the simplest kind of artificial neural network named mono-layer perceptron (or simply, perceptron). In the following we present the probabilistic neural network that is used in this work.

Probabilistic Neural Network is a kind of Artificial Network which is suitable in classifying and identifying the samples. Recently it has been successfully applied in every field of science as a classifier machine. The main and the first step in performing a comparison by the tool is to train the network by training samples. During the training session the network will learn the possible determined classes. The architecture of a probabilistic Neural Network that includes a complete training session is shown in figure 2.9.

When an input vector is fed to the network, the first layer computes the distance from the input vector to the training samples. This produces a vector which indicates how close the input is to the training samples. The second layer sums the contribution for each class of inputs and produces its net output as a vector of probabilities. Finally,

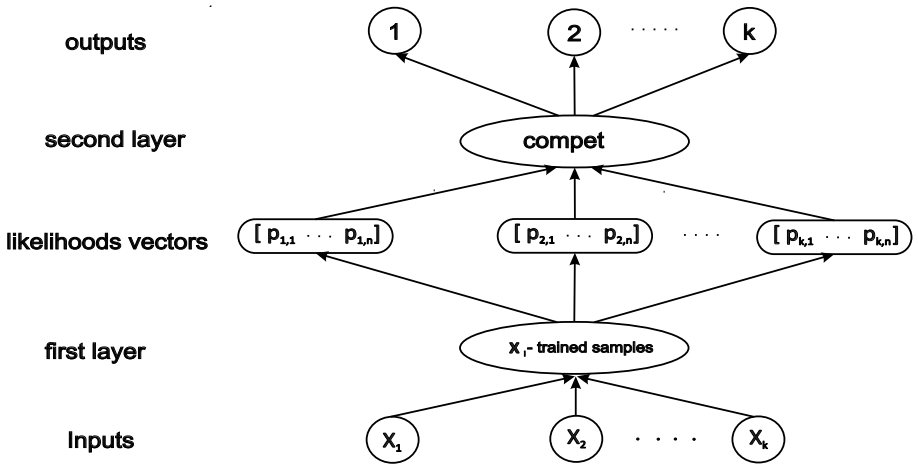


**Figure 2.9:** An Architecture of Probabilistic Neural Network

the Compete transfer function on the output of the second layer picks the maximum of these probabilities and produces 1 (positive identification) for that class and 0 (negative identification) for non-targeted classes. In this way the Network will correspond each tested sample to its own class of trained samples (Bazarghan et al. 2008, Tajfirouze & Safari 2012).

The Probabilistic Neural Network is a supervised algorithm which needs to be trained before being used for classification. Therefore, the greater the number of training samples we provide to feed the network, the more accurate the output of PNN will be. Its performance is based on estimating the probability density function from sample patterns, which implicitly consists of calculating the distances between an input vector with the other training samples. So, it seems to somehow do just like a nearest neighbor classifier (Montana 1992) while comparing to other kind of classification methods. For this reason, it can better deal with irrelevant features.

### 2.3.2 Cross correlation

The other method that we use is cross correlation which is simply a way to measure how similar the signals are. This kind of approach has been recently applied to the analysis of coronal observations (Viall & Klimchuk 2013). Two input vectors of x and y may be cross-correlated as a function of time lag L as:

$$corr_{x,y} = \frac{\sum_{k=0}^{M-|L|-1}(x_{k+|L|} - \overline{\mathbf{x}})(y_k - \overline{\mathbf{y}})}{\sqrt{\sum_{k=0}^{M-1}(x_k - \overline{\mathbf{x}})^2 \sum_{k=0}^{M-1}(y_k - \overline{\mathbf{y}})^2}} \quad \text{for} L < 0 \tag{2.8}$$

$$corr_{x,y} = \frac{\sum_{k=0}^{M-|L|-1}(x_k - \overline{\mathbf{x}})(y_{k+|L|} - \overline{\mathbf{y}})}{\sqrt{\sum_{k=0}^{M-1}(x_k - \overline{\mathbf{x}})^2 \sum_{k=0}^{M-1}(y_k - \overline{\mathbf{y}})^2}} \quad \text{for} L \geq 0 \tag{2.9}$$

where $\bar{x}$ and $\bar{y}$ are the averages of the vectors$x = (x_0, x_1, ..., x_{M-1})$ and $y = (y_0, y_1, ..., y_{M-1})$, respectively ($M$ is the number of data points).

The function $c\_correlate$ within the IDL software enables us to find the correlation values between two selected samples at any given time lag. The highest similarity between two samples will be indicated by the maximum cross correlation value.

## 2.4 Results

For each combination set of the parameters we have a package of 10000 realizations (or 10000 pairs of simulated light curves) . We have also the light curves of a single pixel and a row of neighboring pixel (observed light curves). Next, we want to compare the simulated light curves with the observed ones.

Our key point is to find the realization that best matches the light curves in both channels at the same time.

We initially begin with Probabilistic Neural Network.

### 2.4.1 PNN outputs

With the PNN method we are not able to compare couples of light curves simultaneously, but only one model light curve with one observed light curve at a time. Since we want to match simultaneously light curves in two different channels, our solution has been to join each light curve in one channel to the corresponding light curve in the other channel. So, we first normalize each light curve to its maximum value, and then we stitch the end point of one to the first point of the other. This is done for both the simulated and observed light curves. Afterwards, we trained the network with the simulated light curves as training samples. The observed light curves are then fed the network as the tested samples to classify with respect to the trained samples. The process of classifying the data is done for the light curve of the single and of the row of pixels separately.

The output of the network finds the best choice among the available set of simulated patterns which best resemble the data and labels it with its own corresponding key parameters. For each of the 12 sets of parameters, we show the light curves of the realisation that best matches the observed ones, Fig. 2.10 in a single pixel and Fig. 2.11 in a set of neighboring pixels according to the PNN method. For a better visual comparison, we have applied normalization and shifting procedures. In the case of single pixel light curves we also applied smoothing procedure with a box car of 8 data point. We remark that the PNN compares the realizations with the original light curves (after a normalization only).

In general, the PNN is unable to find simulated patterns that perfectly match the observed ones, not even in one channel. The PNN chooses the best solution as the one that shows the best match of the overall general patterns. As mentioned above, we let

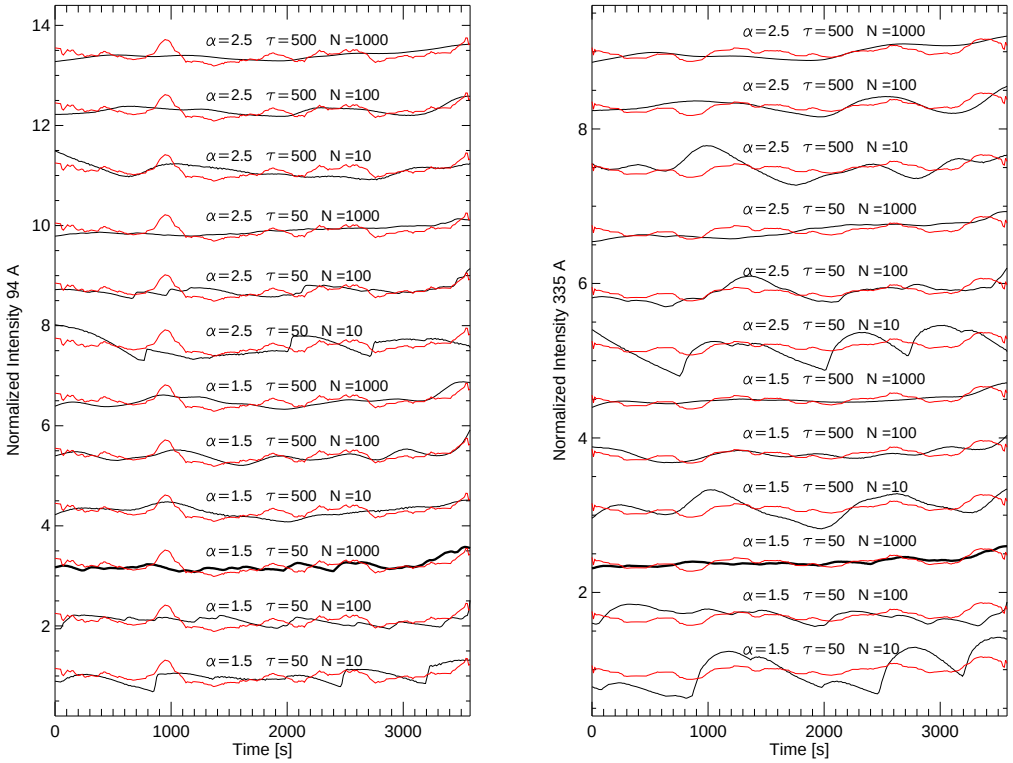


**Figure 2.10:** *Black solid lines:* Light curves from realisations for each set of parameters ($\alpha, \tau$ and N) that best match the observed ones in the single pixel (red lines) according to the PNN method. The light curves in both the 94 Å (left column) and 335 Å (right) channels are shown. Comparison of observed (red lines) light curves to the best model ones (black lines) found by the network for each set of parameters ($\alpha, \tau$ and $N$). For a better visual comparison, the intensities are normalized to the average and shifted each by a different value, and the observed light curves have been smoothed with a boxcar of 8 points. The best absolute match is marked (thick black lines).

the method find the best solution for each set of parameters. It remains to be found the best absolute solution. We might rank the best solution on its overall ability to reproduce the details of the observed features, and in particular the amplitude, shape and time scale of the observed bumps in both channels. From a visual inspection of Fig. 2.10 and Fig. 2.11 we realize that the best solutions are not equivalent. Those with the long pulse duration, with a small number of strands and with a steep distribution all show too broad features, which do not fit the observed features on the smallest time scales, especially in the 94 Å channel. Also the solutions with the steeper distribution ($\alpha = 2.5$) are in general unable to reproduce the variability on short time scale. A small number of strands determines too strong bumps in the 335 Å channel. The best absolute solutions appear those with the flatter energy distribution, and shorter pulse

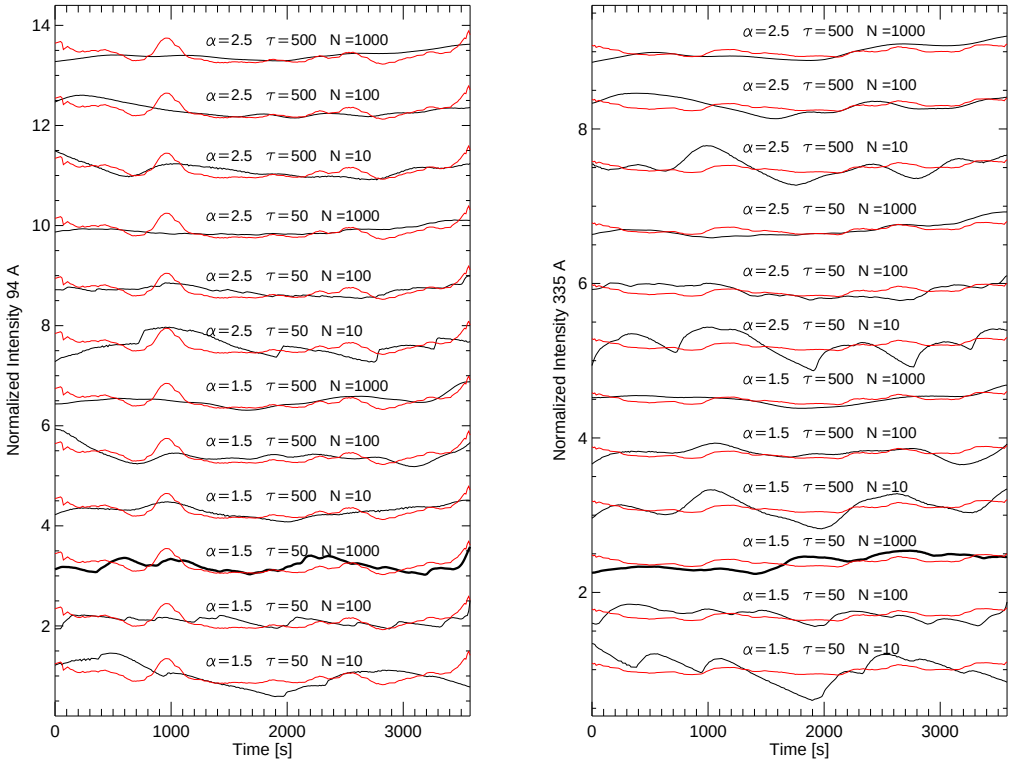


**Figure 2.11:** As Fig 2.10, The comparison for a set of neighboring pixels.

duration. Among these, the one with the largest number of strands yields the lowest total root mean square deviation (RMSD) from the observed light curves defined as:

$$\text{RMSD} = \sqrt{\sum_{i}^{M} \frac{(\overline{R}_i - \overline{O}_i)^2}{M}} \tag{2.10}$$

where $\overline{R}_i$ are the model intensities normalised to their average (for each channel), $\overline{O}_i$ are the observed intensities normalised to their average and M is the number of strands. So, eventually, the best set of parameters found with PNN is [$\alpha = 1.5$, $\tau = 50$ and $N = 1000$] (black lines in Fig. 2.12), for which we obtain RMSD $= 0.15$ in the case of comparison with the light curves of a single pixel and RMSD $= 0.16$ in the case of comparison with the light curves of a set of neighboring pixels.

Two points here are worthy of being pointed out. One is the fact that the network is not sensitive to denoising or smoothing (Tajfirouze & Safari 2012). Another point is that the output of the network does not change even when we reverse the order of stitching the light curves. This means that the network is robust in its performing.

We obtain very similar results when we compare the model realizations with the observed light curves extracted from the row of pixels, i.e. the same best set of param-

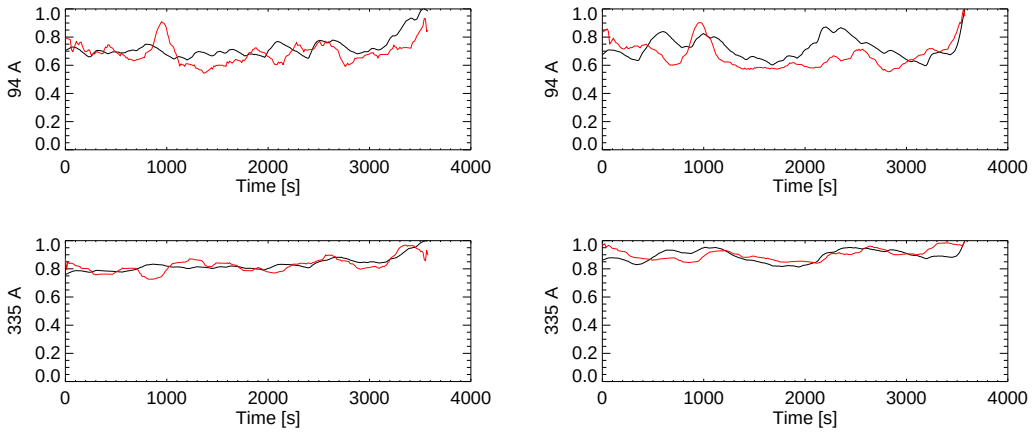


(a) (b)

**Figure 2.12:** Modeled light curves (black lines) in AIA 94 Å channel (upper panels) and 335 Å channel (lower panels) for the case $alpha = 1.5$ $\tau = 50$ $N = 1000$ best matching the observed ones (red lines) from (a) a single pixel and (b) a set of neighboring pixels, found with the PNN method. These are the best absolute match. The model intensities are normalized to their maximum.

eters with both PNN and cross-correlation. From now on, we will consider the best solution found for the single pixel and with the PNN method as the best absolute one.

### 2.4.2 Results with cross correlation technique

We make an alternative comparison using the simple cross-correlation technique described in Section 2.3.2. With this method we can compare the simulated and observed light curves of both channels simultaneously without joining them. In a given channel each model light curve is time-shifted and cross-correlated with the observed one (either the single pixel or the pixel row), and the cross-correlation value is computed. As we did for PNN, we do this for each set of parameters. The best match is given by the realization that provides the highest sum of cross-correlation values found for the two channels and the same time lag. The best matching realisations for each set of parameters found with cross-correlation are shown in figure 2.13 in the case of comparison with observed light curves of single pixel and figure 2.14 in the case of comparison with observed light curves of a set of neighboring pixels.

The best absolute matching (and the highest cross correlation value) are obtained by the same set of parameters as that found with the PNN method, i.e., $\alpha = 1.5$, $\tau = 50$, $N = 1000$, although with a different realisation (black lines in Fig. 2.15). However, for the best realisations we obtain RMSD $= 0.20$ in the case of comparison with the light curves of single pixel and RMSD $= 0.31$ in the case of comparison with the light curves of single pixel, which is higher than that obtained with the PNN

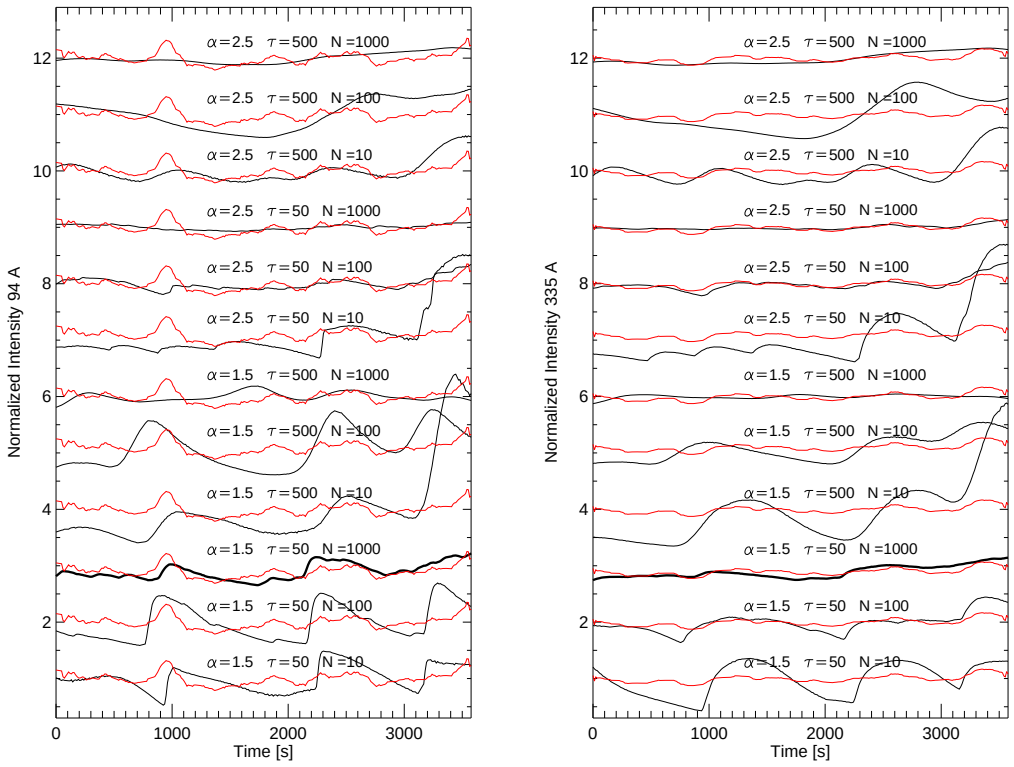


**Figure 2.13:** As for Fig. 2.10, The comparison by Cross correlation technique.

method.

It is interesting to make considerations about the absolute intensity values. We first compare the ratio of the mean observed intensities with those of the best absolute realisation (Figure 2.12a). We obtain $(I_{335}/I_{94})_{obs} \approx 5.1$ vs $(I_{335}/I_{94})_{mod} \approx 5.5$. The agreement is remarkable, the percent difference ($\sim$ 7%) being less than the average fluctuations of the 94 Å light curve ($\sim$ 15%). The slightly higher emission observed in the 335 Å channel might be simply due to some diffuse emission along the line of sight. To report the model results to the observations we have to make an assumption about the cross section of the strands. We find that we need a cross section of 0.56 and 0.52 pixels in the 94 Å and 335 Å channels, respectively, to match the best model to the observed light curves. In the assumption of 1000 equal and independent strands, this is equivalent to find that each strand has thickness of $\sim$ 10 km. This becomes a lower limit if the strands are not entirely independent, i.e., if the same strand is heated more times during our time lapse (see Section 2.2.1). We should also keep in mind that we have a logarithmic spacing in our sampling of the number of strands, and therefore this value of the thickness should be taken with care.

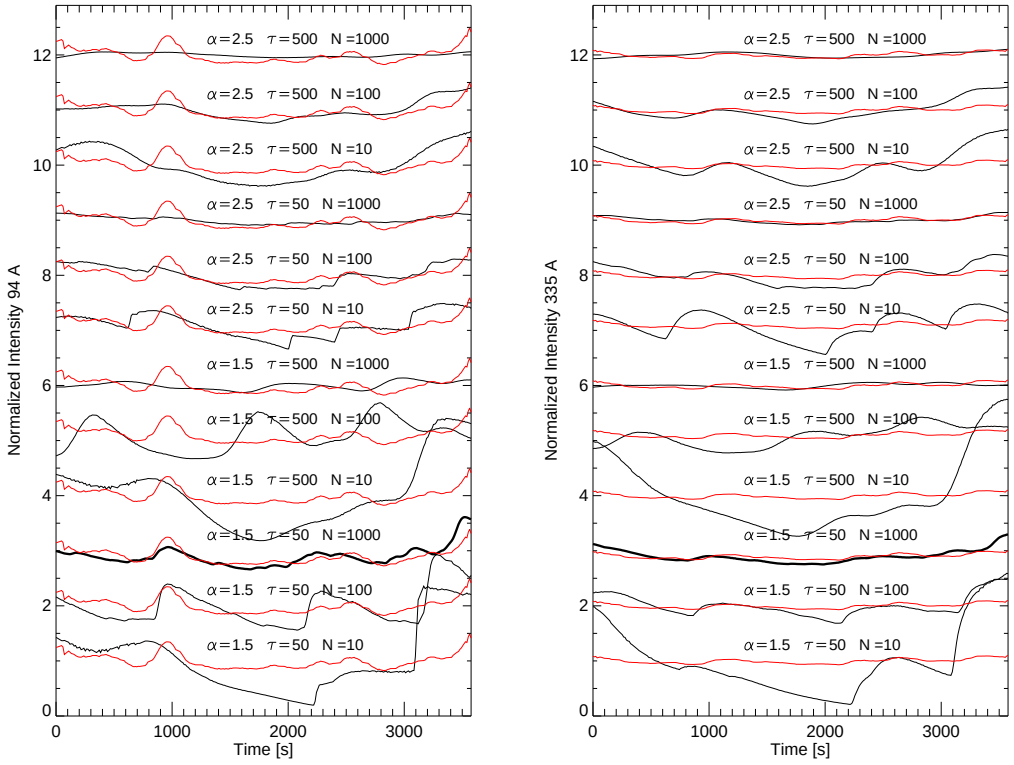


(a) (b)

**Figure 2.14:** As for Fig. 2.11, The comparison by Cross correlation technique.

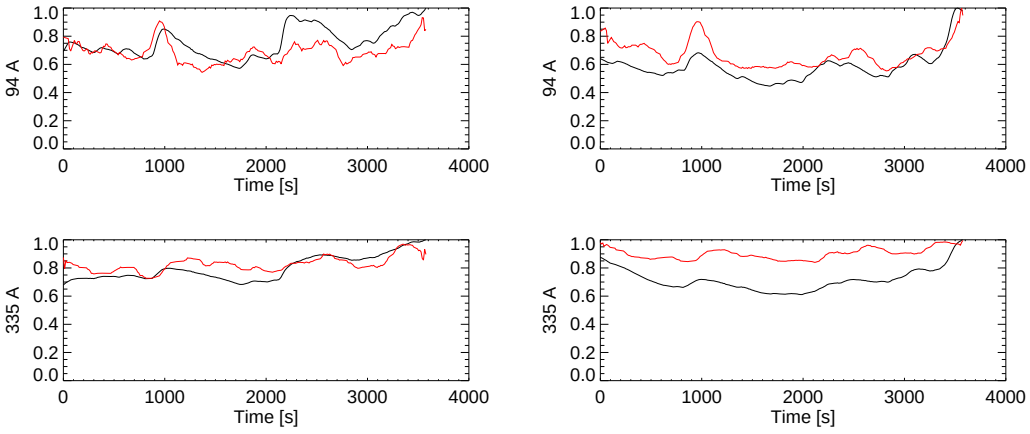


(a) (b)

**Figure 2.15:** As for Fig.2.12, the best absolute match found by cross correlation technique.

## 2.5 Discussion

In this work we analyse the time evolution of the EUV emission in the core of an active region, which shows evidence for a very hot ($T > 5$ MK) plasma component

(Reale et al. 2011). This hot component might be a signature of the occurrence of rapid but intense heating releases, which bring the plasma to such high temperature for short times. In that active region we consider the light curves at the maximum time resolution in three SDO/AIA channels picked up either in a single pixel or in a row of pixels where the emission evolves coherently.

We try to match the observed light curves with the emission derived from specific loop modelling. The simultaneous presence of very hot plasma and steady emission indicates that we might have storms of events with a broad range of energy distribution.

In the light of this evidence, our choice has been to describe the evolution in a scenario of loops made by bundles of independent strands each heated for a time shorter than the typical plasma cooling times (e.g., Guarrasi et al. 2010). We assume that each strand is tenuous and cool at the beginning and is heated only once, at a random time, by a heat pulse of random intensity. It is then left free to decay. This is equivalent to fewer strands heated repeatedly but not at high frequency, i.e., after time intervals longer than the cooling and draining times (Warren et al. 2010b; Klimchuk 2015, see also Section 2.2.1).

Since we address the time evolution only, and no spatial issues, we preferred to consider the very efficient approach of 0D loop modelling, that describes the evolution of the average quantities of the coronal plasma contained in a loop magnetic flux tube. The output of the model is the evolution of the average density and temperature, that we use to derive the light curves in relevant channels to be compared with the observed ones. An important issue is the choice of the free parameters. We assume that all strands have the same length, which is constrained from the observation. We observe mostly straight bright structures in the core of the active region deep in the disk, so we assume semicircular strands that stand vertically from the surface. The other important parameters are the intensity of the heat pulses, their duration and the number of strands. In the framework of randomly occurring events, we assume that the heat pulses are distributed as power laws. We assume two possible values of the power law index, i.e. a shallower ($\alpha = 1.5$) and a steeper ($\alpha = 2.5$) one.

We then normalize the intensity and range of the distribution so to have an average heating rate that is able to produce a loop plasma at 3 MK on average, according to the loop scaling laws. We set two possible duration of the heat pulses, a short (50 s) and a long (500 s) one. The number of strands changes logarithmically, from a few (10), to a relatively large number (1000). For each of the two pulse distributions with different $\alpha$ and of the two pulse durations, we generate a grid of 0D models. For each model we derive the light curves in the AIA 94 Å and 335 Å channels. The next step has been to choose a number of strands and to combine randomly the corresponding number of light curves in a channel, according to one of the pulse distributions and for one pulse duration. So we randomly pick up an intensity from the intensity distribution, and a random start time of the pulse, uniformly distributed in a time range of 10000 s. For each set of parameters we derive 10,000 different realisations, i.e. random combina-

tions of light curves in the 94 Å and 335 Å channels. Each couple of light curves has been compared to the couple of the observed ones. The comparison has been made independently with two different methods, one based on artificial intelligence, the other on a simple cross-correlation. We do not address a perfect match of the simulated and observed light curves, that would require much larger sets of realisations. We let the methods find the best realisations for each set of the parameters. Then, we compare these best cases and pick up the one that is able to reproduce patterns globally similar to the observed ones, and in particular variations with similar amplitude and timescales and similar shapes of the local emission bumps or dips.

The parameter set of the realisation that best matches qualitatively and quantitatively the observed light curves is a shallow power law index ($\alpha = 1.5$), a short pulse duration (50 s) and relatively large number of strands (1000). This realisation has been singled out with the PNN method, minimizes the deviations from the observational data, is able to reproduce well many features of the observed light curves, and delivers a ratio of the intensities that is consistent with the observed ones. Realisations with the same set of parameters best match the light curves both of the single pixel and of those averaged over a row of a few pixels.

The distribution of events is able to describe the presence of both many weak and few strong events, that explain both the rather smooth light curves and the presence of a small amount of hot plasma at the same time. The relatively small duration of the heating release, of the order of 1 minute, is in agreement with recent finding from observations and modelling (Testa et al. 2013, Testa et al. 2014). A relatively high number of heated strands is preferred, and is able to reproduce well the rather steady emission. We find that the intensities from this combination of parameters are compatible with strands $\sim 10$ km thick or more, to be compared with recent measurements ($\sim 100$ km) from high resolution observations (Brooks et al. 2013).

The simulated light curves that best match the observed ones show that the emission fluctuates more in the 94 Å channel, and it is smoother in the 335 Å channel, which is more sensitive to cooler plasma. However, we can see a large scale similarity in the global trends.

Figure 2.16 shows the evolution of the plasma and heating event properties for all the modeled strands (In the case of best absolute match for a single pixel light curve found by network). In the temperature plot, among the multitude of lower temperature events, we clearly distinguish a smaller number of events that bring the temperature above 10 MK for short times. They are consistent with the detection of a small and filamented amount of very hot plasma in this region (Reale et al. 2011). It is interesting to search for signatures of physical processes in the light curves. Figure 2.17 zooms in a 1000 s time range of Fig. 2.16 and shows the temperature events, the distribution of heat pulses and the evolution of the average event heating rate, with a 50 s time binning.

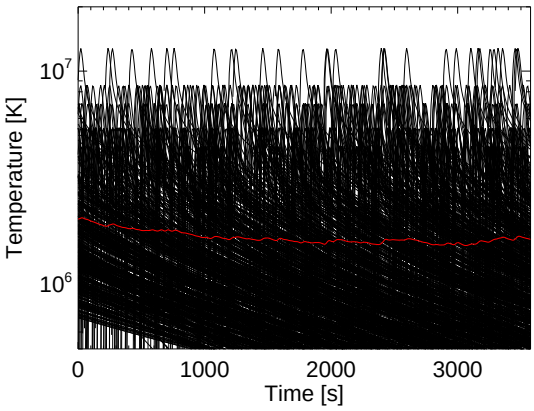


(a)

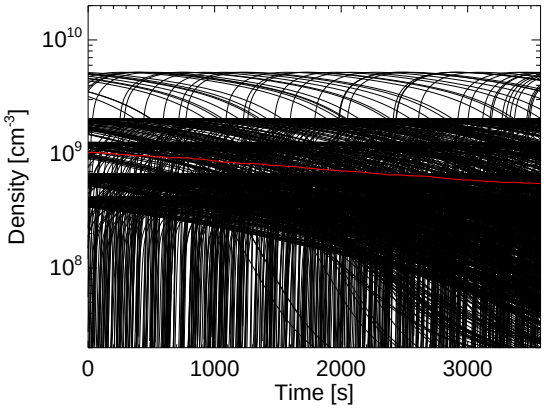


(b)

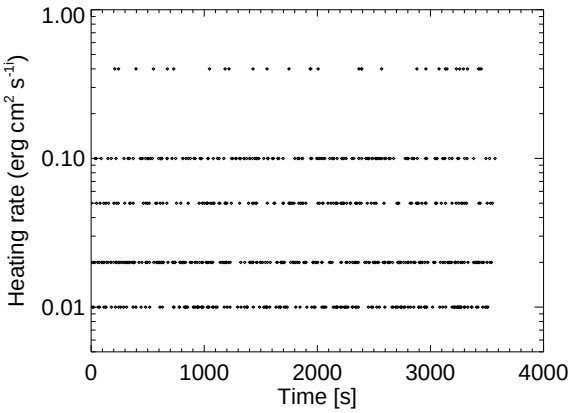


(c)

**Figure 2.16:** Time evolution of (a) temperature, (b) density and (c) heat pulses of all the randomly heated strands that overlap to build the model light curve (of a single pixel)in Fig. 2.12a. The red lines are the average values. Time has been shifted by 1800 s.

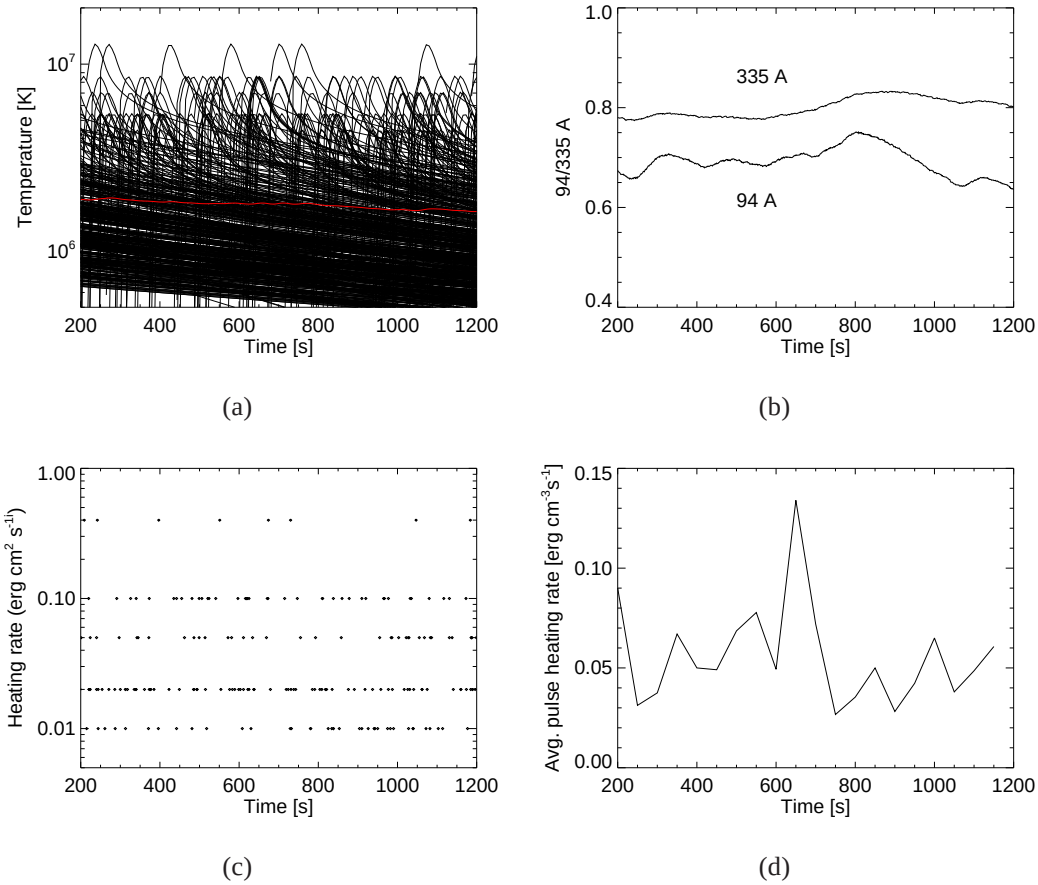


**Figure 2.17:** Enlargement of Fig. 2.16 in a time range of 1000 s, showing (a) temperature, (b) intensity of 94 Å, and 335 Å (see Fig. 2.12a), (c) the heat pulses and (d) the average heat rate of each pulse over bins of 50 s.

While we do not see any obvious correspondence between the light curves and the first two quantities, we clearly see a correlation of the event heating rate with the trends observed in the light curves. In particular, we see a train of heat bumps that anticipates a train of emission bumps by $\sim 200$ s in the 94 Å channel. This time lag is of the same order as the delay between the temperature peak and the emission peak for a single strand shown in Fig. 2.4a,c (see also Section 2.2.1), ultimately due to the more gradual evolution of the density. We might therefore infer that strong fluctuations in the 94 Å channel probably mark a previous increment of heating episodes with a delay of a few minutes. This signature is present also in the 335 Å channel, but is much less significant.

Overall, the analysis presented here shows results that are consistent with previous works. The short and infrequent heat pulses are largely consistent with the presence of cooling plasma for most of the time, which was detected in Hinode/XRT observations (Terzo et al. 2010) and in SDO/AIA observations (Viall & Klimchuk 2012). In the former work a good match with observations is obtained with Monte Carlo simulations

including most energetic random pulses at average time distance of 360 s from each other. From Fig. 2.17 we can count a number of $\sim 30$ highest pulses (0.4 erg cm$^{-3}$ s$^{-1}$, with comparable peak temperature and duration with those in Terzo et al. 2010) in $\sim 1200$ s, corresponding to an average time distance of $\sim 150$ s. This higher frequency is not included in Terzo et al. (2010) and might be consistent for the core of an intense active region. The model also involves the presence of very hot plasma as detected in the same region analysed here in SDO/AIA observations (Reale et al. 2011). Our analysis obtains additional information about the number, distribution and intensity of the heating events and about the fine loop structuring, and figures out possible signature of the heating directly detectable in the light curves.

This works improves also on the previous analysis with artificial intelligence methods (Tajfirouze & Safari 2012), because we use specifically a loop model as basic model, because we address simultaneous match of the light curves in two different channels, and because we cross-check with a different comparison method, namely cross-correlation.

A further improvement on our analysis could be the attempt to include also some spatial information, i.e. the coherence of the signals in the same loop structures. This requires using more detailed loop models that describe the confined plasma with spatial resolution. The nest chapter will be devoted to explore this issue.

# Chapter 3

# Space Resolved Analysis of pixels region

## 3.1 The question and the approach

In the previous Chapter, the analysis of observations in the EUV band has shown that a storm of heat pulses in a coronal loop is able to explain steady but flickering light curves in single spatial elements (Tajfirouze et al. 2015). A 0D loop model (EBTEL Klimchuk et al. 2008; Cargill et al. 2012) that computes average loop quantities with no spatial resolution was used with success to produce a grid of simulations of pulse-heated strands with different heating rates and two basic durations, namely 50 s and 500 s, the latter comparable to plasma cooling times. We assumed a power-law energy distribution of the pulses and three possible number of independent strands, i.e. 10, 100 and 1000. In the assumption of active region loops made of bundles of strands, we then combined the pulse-heated model strands with random energy and random start times of the heat pulses into 10000 realisations for each set of parameters. An artificial intelligence method allowed to find a realisation that best reproduces the observation in two EUV channels. This realisation was labeled with a shallow power law frequency distribution ($\alpha$= 1.5) of the heat pulses, the short pulse duration (50 s), and the largest number of strands (1000).

Here we use the best realisation of the previous work (see., Tajfirouze et al. 2015) which was able to reproduce properly the observed features of a single pixel in the EUV band, as reference model to investigate a more detailed issue related to the active region coronal loops. We study how the temporal evolution of the emission changes with the spatial location along the loops. To do this, we need a model with spatial resolution so we move from 0D to 1D loop modeling. We will freeze the model parameters to those of the previous work and explore the spatial dependence determined by this parameter combination and possible diagnostics that we will compare to the observation.

## 3.2 One Dimensional Loop Model

We use Palermo-Harvard code, One-dimensional time-dependent loop model (Peres et al. 1982; Betta et al. 2001), which considers the magnetic field as static and solves the hydrodynamic equations for a toroidal geometry with constant cross section along one representative strand using an assumed heating rate.

The differential fluid equations of conservation of mass, momentum and energy are:

$$\begin{aligned}
\frac{dn}{dt} &= -n\frac{\partial}{\partial s}(v) \\
nm_H\frac{dv}{dt} &= -\frac{\partial}{\partial s}P + nm_H g + \frac{\partial}{\partial s}(\mu\frac{\partial v}{\partial s}) \\
\frac{d\zeta}{dt} + w\frac{\partial v}{\partial s} &= E_H - n^2\beta P(T) + \mu(\frac{\partial v}{\partial s})^2 - \frac{\partial}{\partial s}(\kappa\frac{\partial T}{\partial s}) \\
p &= (1+\beta)nk_BT \\
\zeta &= \frac{3}{2}(1+\beta)nk_BT + n\beta\chi \\
w &= \frac{5}{2}(1+\beta)nk_BT + n\beta\chi
\end{aligned} \tag{3.1}$$

where $n$ is the hydrogen number density, $v$ the plasma bulk speed, $m_H$ the hydrogen atom mass, $g$ the local gravitational acceleration, $s$ the field line coordinate ($s_0 \equiv$ location of temperature minimum $= 4.5 \times 10^4\ cm$, $s_{max} \equiv$ location of temperature maximum $= 2 \times 10^9\ cm$). $\mu$ the effective plasma viscosity, $\beta$ the fractional ionization $n_e/n_H$ (viz., Brown 1973), $k_B$ the boltzmann constant, $P(T)$ the radiative loss function (identical to that of Rosner et al. (1978) for $T > 2\times10^4$, and for $T < 10^4$ derived from the Vernazza et al. (1981) atmosphere model), $T$ the plasma temperature $\kappa$ the thermal conduction coefficient (Spitzer 1962), $\chi$ the hydrogen ionization potential, and $E_H$ is assumed to be uniform in the corona (without any attempt at modeling its functional dependence on plasma density and temperature ), and is derived from the (Vernazza et al. 1981) models for the chromosphere.

The above equations are approximated with finite difference equations and are solved on an adaptive grid, the number and the spatial size of which is modified at each step of time integration to resolve properly the steep transition region especially at the beginning of a flare. As shown in Betta et al. (1997), a good resolution in the transition region may also influence the solution in the corona; in fact, the evaluation of the conductive flux and mass motions in the transition region also determines the quality of the results in the rest of the atmosphere. The code allows for including both the spatial and temporal dependencies in the heating term.

The Palermo-Harvard code in particular, has been extensively applied to many problems of coronal physics, including studies of loop stability, analysis of physical processes influencing the thermal flare (Pallavicini et al. 1983; Peres & Reale 1993a,b;

Reale & Peres 1995), diagnostics of the location of the energy release in solar flares (Peres et al. 1987; Antonucci et al. 1987, 1993); the code has also been used to model a stellar flare observed by the Einstein satellite (Reale et al. 1988) allowing to infer the characteristic length of the flaring structure, to study the decay phase of solar (Serio et al. 1991; Jakimiec et al. 1992; Sylwester et al. 1993) and stellar flares (Reale et al. 1993), in order to devise diagnostics of flare conditions from the decay phase, and to study microflares (Peres et al. 1993).

As we did in Chapter 2 with EBTEL model, we let a single strand evolve under the effect of a heat deposition uniformly distributed along the strand. The details of the heat deposition are important in the initial phases of the evolution, but much less over the longer time scales of our interest, when the plasma quickly loses memory of the previous evolution. The model computes the evolution of the density, temperature, and velocity of the plasma along the single coordinate of the loop. The initial cool and tenuous atmosphere is kept steady by a low constant heating of $0.23 \times 10^{-4}\ erg\ cm^{-3}s^{-1}$ which supports a pressure of $0.018\ dyn\ cm^{-2}$ and a temperature of $0.62\ MK$ in a semicircular loop of half length $\sim 2.5 \times 10^{9}\ cm$.

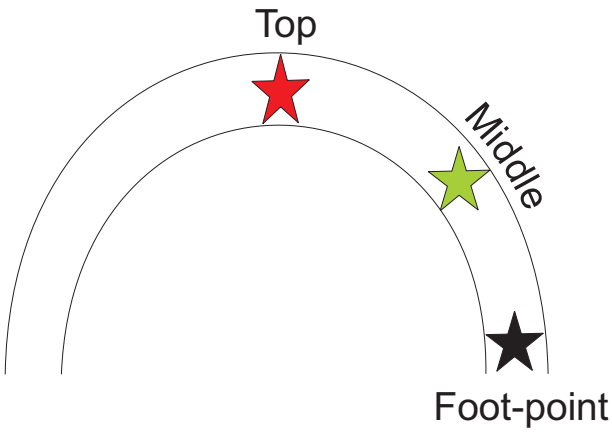


**Figure 3.1:** The scheme of an individual strand. Red, green and black stars respectively point to the top, middle and the footpoint of the loop.

The evolution of the loop plasma under the effect of a single heat pulse is well known from previous work (e.g. Cargill 1994; Cargill & Klimchuk 2004; Bradshaw & Cargill 2006; Reale & Orlando 2008; Guarrasi et al. 2010). Figure 3.2 shows the evolution of the density and temperature at three representative positions (top, middle, footpoint (see figure 3.1 ))of a single strand as the relaxed loop atmosphere is perturbed by a heat pulse with a triangular time evolution and a peak intensity of $h = 0.003$ erg cm$^{-3}$ s$^{-1}$ and with a total duration of $\tau = 50$ s.

As expected, the overall evolution is similar to that of the single strand shown in Chapter 2 (see also., Tajfirouze et al. 2015). Again we see a steep temperature rise and a slower decay, and a slower evolution of the density. The evolution is very similar at all positions, except for a shift to higher temperature and to lower density toward

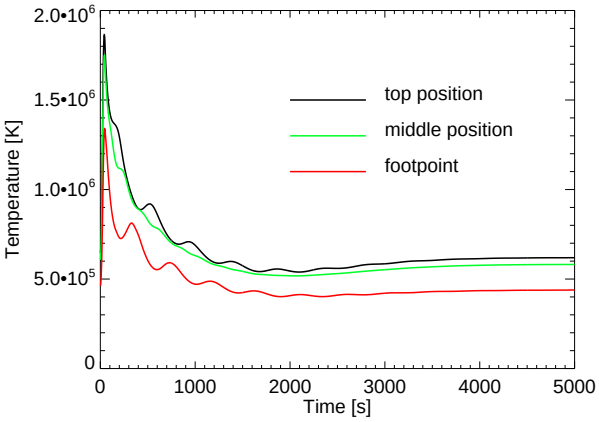


(a)

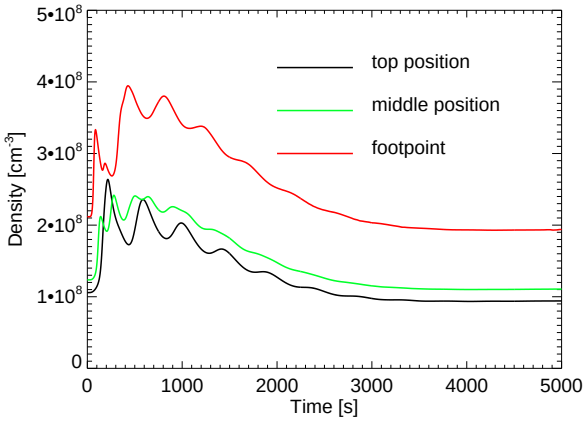


(b)

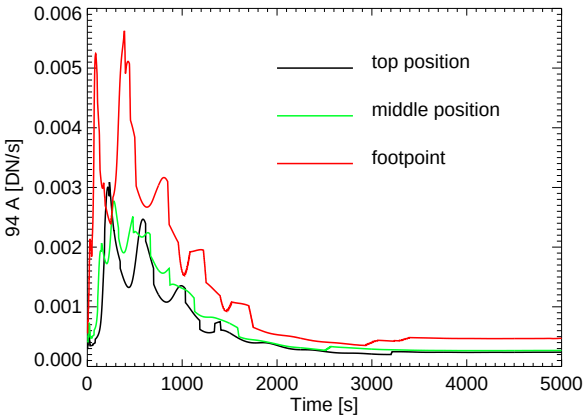


(c)

**Figure 3.2:** Evolution of (a) Density (b) Temperature (c) and Intensity in 94 Å channel at 3 different locations along a pulse-heated strand.

the strand top, as expected from temperature and density stratification. Figure 3.2 also shows periodic fluctuations in both quantities and at all positions. These are due to pressure waves that travel back and forth along the strand triggered by the highly discontinuous heating. The maximum temperature at the top is close to 2 MK, and the density reaches around $5 \times 10^8$ cm$^{-3}$ close to the footpoints. As in previous Chapter, we assume that each strand is heated only once by a single pulse whose energy and power are selected at random from a power-law distribution.

Using the outputs of 1D hydrodynamic model we can derive the emission at any time from single positions along the strand as $n(s,t)^2 G[T(s,t)]$ (see also appendix A)where $s, t$ are the spatial and temporal coordinates, respectively, $n$ is the density, $T$ is the temperature, $G(T)$ is the instrument sensitivity function to plasma emitting at temperature $T$. In this work we consider the emission as observed in the 94 Å and 335 Å EUV channels of the Atmospheric Imaging Assembly (AIA) on-board the Solar Dynamics Observatory (SDO). These channels are best sensitive to plasma at $\sim 4-6$ MK, and $\sim 3$ MK respectively, in the core of an active region. Figure 3.2 also shows the expected emission in the 94 Å channel, which has an intermediate evolution between the temperature and the density. We see here larger periodic fluctuations with respect to those of temperature and density, but these will be mostly washed out when we will randomly combine the light curves of a bundle of strands.

## 3.3 Analysis and Results

We generate the same grid of strand models for the short duration heat pulses as we did in Chapter 2, i.e. the same sampling of the energy range, and we combine them with the same population, distribution and starting times as the most successful realisation (recognized by PNN). As mentioned in Section 3.1, the energy distribution is a power law with index $\alpha = 1.5$, and we extract 1000 strand models, which we overlap with exactly the same sequence as in Chapter 2 in the time range of 10000 s. Whereas in Chapter 2 we summed the average loop emission of single strands to obtain a single light curve, here we sum the space-resolved emission along the strand, i.e. assuming that all strands are parallel and start and end at exactly the same locations on the solar surface. The plasma distribution is rather smooth along the strands and therefore no significant changes are expected for small shifts of one strand to the other.

Figure 3.3 shows the reconstruction of the realization marked by PNN as the best absolute match to the observed one in a single pixel by Palermo Harward code.

We have also attempted to produce the best absolute match made from 1000 heated strands at different positions along the loop. Each position consists of a box of fibrils. The dimension of each box was properly comparable to that of a single pixel.

Figure 3.4 shows the light curves in the 94 Å and 335 Å channels at 15 positions along the loop. As in Chapter 2 the light curves in the 94 Å channels are more variable

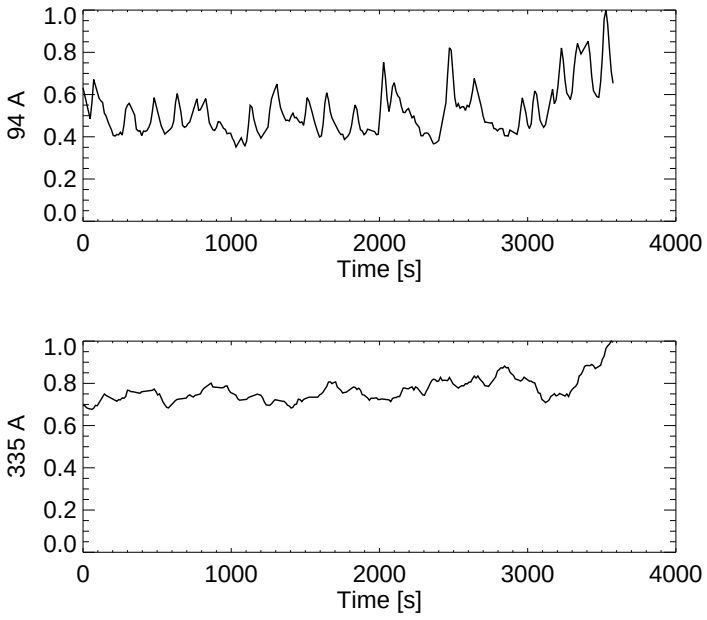


**Figure 3.3:** The best absolute match (see Fig. 2.12a) reconstructed by Palermo Harward code.

and show frequent peaks, because this channel is sensitive to hotter plasma, and therefore to the fast heat pulses. Some of the peaks are due to fluctuations like those shown in Fig. 3.2c. In the 335 Å channels we see smoother light curves. However, space resolution allows us to notice that the light curves in the same channel are similar from one location to the other along the loop, and show no obvious correlation to the light curves in the other channel. In the 94 Å channel we also clearly see that the amplitude of the fluctuations of the light curves increases moving from the base to the top of the loop. The opposite occurs in the 335 Å channel: the fluctuations increase from the top to the footpoints. This is not only a visual impression; we measured the standard deviation from the average of each light curve and it grows upwards in the 94 Å channel and downwards in the 335 Å channel, thus showing the same trends quantitatively. This means that we expect more flickering of the emission going to the top of the core loops in the 94 Å channel, and to base in the 335 Å channel. We have investigated the reason for this behaviour, which is not obvious because we are looking at the sum of a multitude of contributions.

A hint can be found examining the brightest strands that contribute to the emission in the two channels. We have checked that the 94 Å channel is sensitive to the hottest plasma at the top of the strands. The hottest strands are also those with the largest emission measure, they are the fewest according to the power law, and they stay very hot for a small time. For these reasons the channel is extremely sensitive to their variations, and in particular to plasma entering and exiting its temperature response at the top of the hottest strands. Since the temperature in each strand decreases downwards

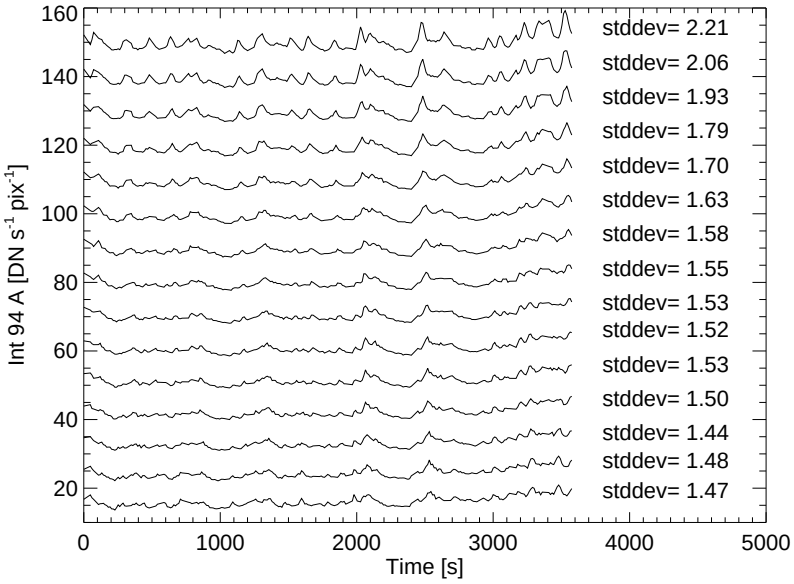


(a)

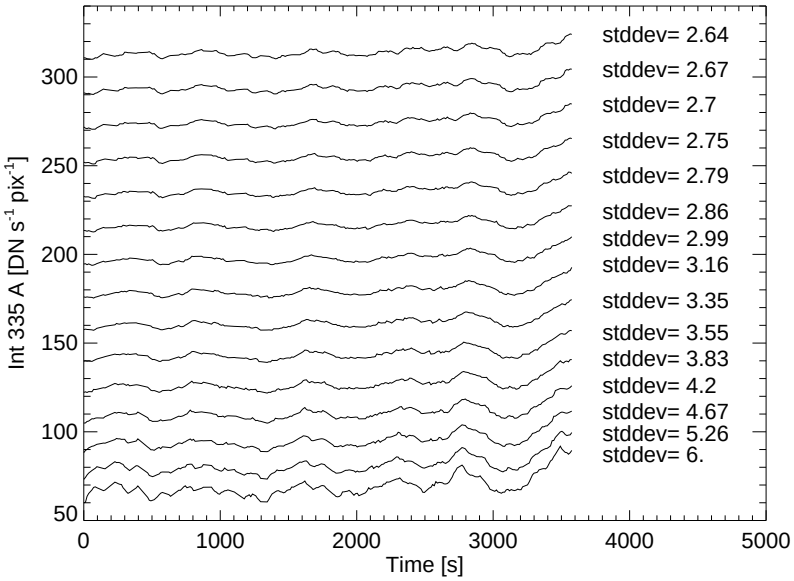


(b)

**Figure 3.4:** Model light curves along the loop for the 94 Å (left) and 335 Å (right) channel. The lightcurves from the bottom to the top of the plot are for locations from closer to the footpoints to closer to the loop top, and are shifted by a constant positive value from the bottom one (10 and 20 DN $s^{-1}$ $pixel^{-1}$ for the 94 Å and 335 Å channel, respectively). Corresponding values of the standard deviations from the mean are reported on the right of each curve.

to the loop footpoints, the same strands lead to the same effect in the 335 Å channel at the loop footpoints. Fig 3.5 shows the histograms of the emitting strand along the loop

and confirms that the 94 Å one has a long tail to the high emission side at the top and not elsewhere, the 335 Å one at the footpoint. These strands in the tail determine the larger fluctuations in the two channels.

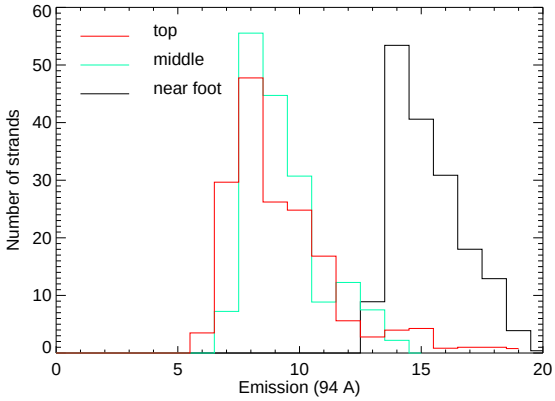


(a)

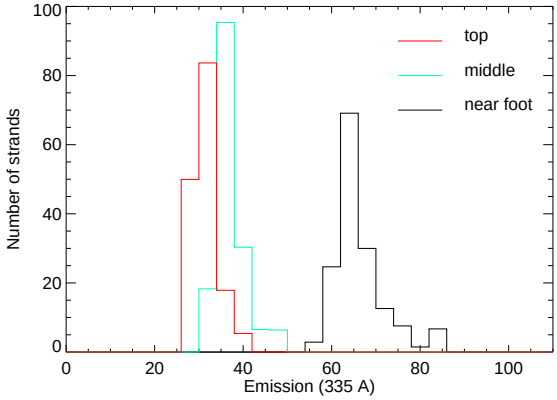


(b)

**Figure 3.5:** Histograms of the emitting strands vs emission intensity (DN $s^{-1}$ $pix^{-1}$) in the 94 Å channel (a) and 335 Å channel (b) at three different locations along the modelled loop, top (red), middle (green) and footpoints (black). High emission tails are present at the top in the 94 Å channel and at the footpoint in the 335 Å channel.

As a feedback to the data, we have searched for a similar behavior in the observations. We consider the same observation of AR11117 on 2010 October 28 as in Reale et al. (2011), and, in particular, the same sequence of 246 and 228 co-aligned images in the 94 Å and 335 Å channel, respectively, as in Previous Chapter, for a total duration of $\sim$ 1 hour. The images are at full space resolution with an exposure time is 2.9 s in both channels. The time distance between the images is 12 seconds, with some gaps up to $\sim$ 1 minute.

We have selected a row of neighbouring pixels among those showing evidence for super-hot plasma in the core of the active region (Reale et al. 2011). Actually, we

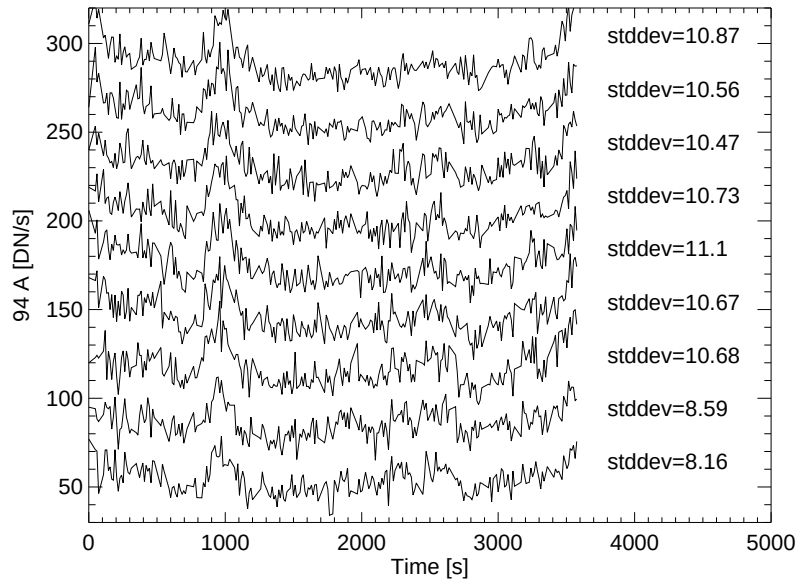


(a)

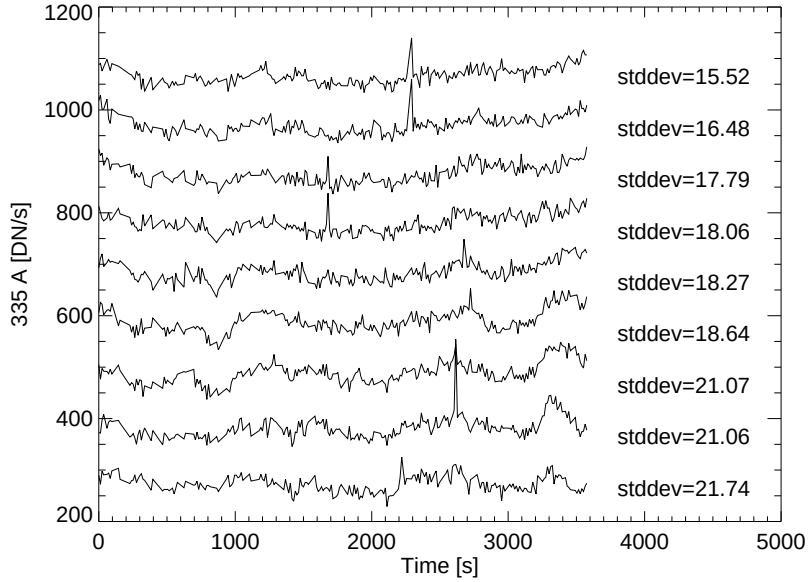


(b)

**Figure 3.6:** Observed light curves in neighbouring pixels in a row for 94 Å (left) and 335 Å (right) channel. Bottom-up roughly proceeds from closer to the loop footpoints to closer to the loop top, i.e. left to right in Fig. 3.7. The light curves are shifted by a constant positive value from the bottom one (30 and 100 DN $s^{-1}$ for the 94 Å and 335 Å channel, respectively). Corresponding values of the standard deviations are reported on the right of each curve.

have identified a few rows and columns of pixels where the emission shows a coherent time behaviour, i.e. they probably intercept the same loop strands where the confined

plasma evolves coherently. As a representative case we consider the same row of pixels as Chapter 2 (Fig 2.2). The row contains 9 pixels, i.e. the projected length is $\sim 3.8 \times 10^9$ cm, about 1/4 of our loop half length projected on the disk. It is not very important to localise exactly which section of the observed loop we are considering, we only ascertain that the loop section taken by the row is all on one side of the loop (left side) with respect to the apex, and does not contain the loop apex. Figure 3.6 shows the light curves in the 94 Å and 335 Å channels (the third one from the bottom is the single pixel one shown in figure 2.3).

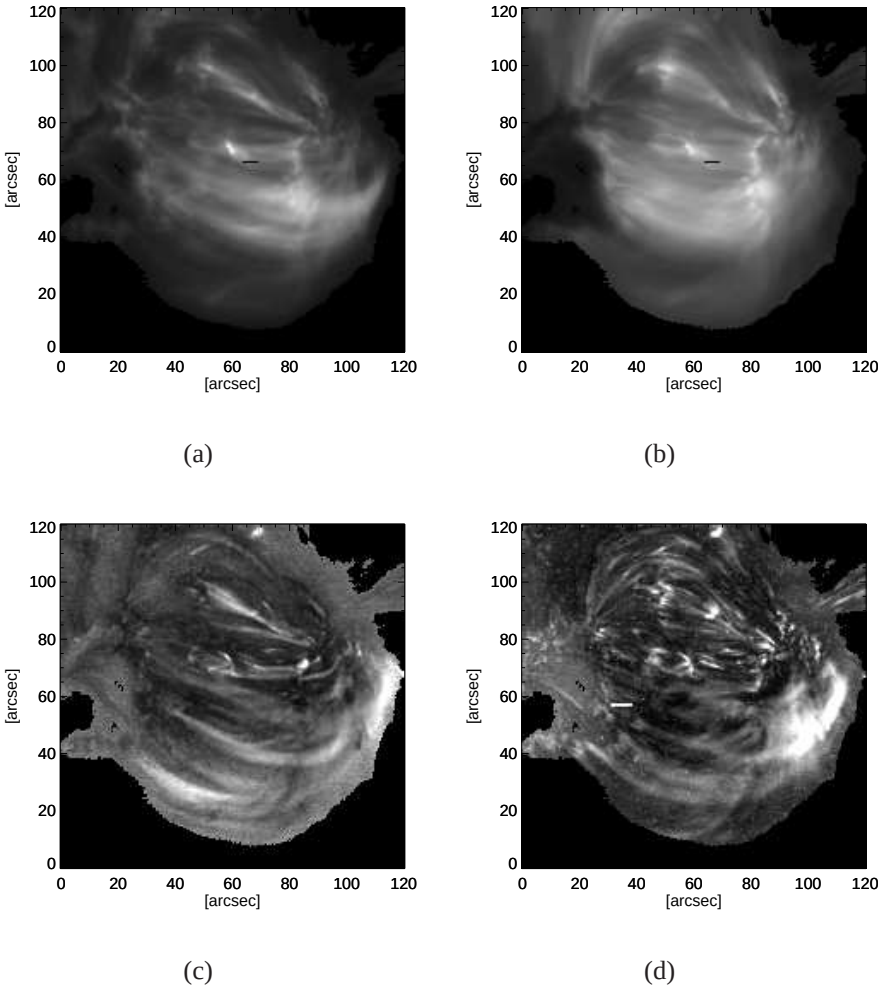


**Figure 3.7:** Core of the active region as observed in the 94 Å (a) and 335 Å (b) channels. Only the region above a signal threshold (10 DN $s^{-1}$ $pixel^{-1}$) in the 94 Å channel is shown. The black segments mark the row of pixels whose light curves are shown in Fig. 3.6. Maps of standard deviation (normalised to the average) in the 94 Å (c) and 335 Å (d) channel. In the 335 Å channel the bright row around [X,Y]=[40,60] is not a real feature, but it is a one-pixel spike that drifts rightwards after co-alignment.

One might then wonder how general these results are. Fig. 3.7 is devoted to answer this question. Together with the images of the core of the active region in the 94 Å and

335 Å channel, it shows respective maps of standard deviation $\sigma$ (normalised to the average map for each channel). The $\sigma$-maps are nicely complementary: the body of many loops are better visible in the 94 Å channel, the footpoints in the 335 Å channel. This confirms larger fluctuations at the footpoints in the "cooler" channel and at the apex in the "hotter" channel in a significant part of the active region core. The similar emission distribution in the intensity maps of the two channels (Fig. 3.7a,b) shows that this effect is not caused by data statistics. As in the model light curves, in each channel the observed light curves are essentially synchronous within our time resolution, with very similar features and bumps that occur at the same time from one pixel to the other. However, already from a visual inspection, e.g. by comparing the top and bottom light curves, we realise that the amplitude of the fluctuations follow a well-defined trend: they increase going from the bottom to the top in the 94 Å channel, and viceversa in the 335 Å channel. These trends are confirmed quantitatively by comparing the standard deviations of all light curves, which are shown on the right of each curve in Fig. 3.6. These trends are the same as found from our modeling. We have also checked that in other randomly selected rows of pixels out of the active region core, the trends are different: we do not find opposite trends in the two channels.

## 3.4 Discussion

Our work shows that a model of finely-structured stranded loop with randomly distributed nanoflares with a power-law energy distribution predicts larger flickering of pixels near the top of the loop in the 94 Å channel, and near the footpoints in the 335 Å channel, at least in active region cores. The difference is due to the different sensitivity of the two channels to the temperature of the emitting plasma, to higher temperature in the former channel (at least in the core of active regions). Therefore, we expect that this effect is not strictly linked to the specific channel, but any bandpasses sensitive to plasma at temperatures roughly above and below 4 MK should show the same trends. The prediction is largely confirmed in the observation of an active region core with evidence for super-hot plasma found in Reale et al. (2011), which is a possible signature of impulsive heating. The presence of fluctuations is intrinsic to the assumption of a highly structured heating, which leads to a multi-thermal and variable emission. The correspondence between large fluctuations at the loop footpoints in the cooler channel and at the loop top in the hotter channel is also a quantitative validation of the temperature and heating rates included in the model. Therefore, this result further supports the model of multi-stranded pulse-heated coronal loop in the active region cores. In the end, we have found an easy diagnostics of structured heating, which might be useful for extensive application to time sequences of full-disk observations. Further work is necessary to investigate the origin and location of the impulsive heating wherever present.

# Chapter 4

# Conclusion

In the first part of this work a combination of field-aligned hydrodynamic modeling and observations from Solar Dynamics Observatory was used to provide additional evidence that the solar corona is heated by impulsive nanoflares. In the second part we introduced a flickering behavior of coronal loops as a new diagnostic of coronal heating. To do this we focused on an active region with evidence of very hot plasma. First we made the light curves of single spatial elements of an EUV detector and compare them to those obtained from a random combination of loop models.

According to impulsive heating scenario in which the heat pulses in the coronal loops are released at constituent fundamental elements, we used a 0D loop model which has no spatial resolution to study the temporal evolution of the magnetically confined plasma. Once we modeled the evolution for such an un-resolved elementary fibril, we derived the emission in two EUV channels, namely the 94Å and 335Å channels imaged by the Atmospheric Imaging Assembly. In a framework that a single pixel contains tens to several hundreds of strands that are intercepted along the line of sight, we simulated the light curve of single pixels by summing over the intensities of the involving strands. Each strand is characterised by a random start time of ignition (from a uniform distribution) and a random energy pulse (from a power law frequency distribution). A grid of strand models was created, so that the included key parameters (power law index $\alpha$, heat pulse duration $\tau$, and the number of strands $N$) span reasonably all the loop conditions in the power law energy range. For each combination sets of the key parameters we made a package of 10000 pairs of light curves.

The simulated light curves were then compared to those of observed in the EUV by Probabilistic Neural Network and separately by cross correlation technique. The realization that was found by PNN as the best absolute match was labeled by the same parameters as was found by cross-correlation. The best absolute match was marked with a shallow power-law ($\alpha = 1.5$), a short duration of the heat pulses ($\tau = 50$) and large number of strands (N=1000). The shallow distribution is able to explain the simultaneous presence of very hot plasma and steady emission. The short duration of the heat pulses ($\sim$ 1 minute) agrees to previous analysis (Testa et al. 2013, 2014).

The largest number of strands is able to reproduce the patterns having rather steady emission.

In the second part of this work we examined the the spatial dependence of the emission variability on the position along the loops. After freezing the heating features from the best match obtained in the first part, we replicated the modeling using a 1D hydrodynamic loop model that could resolve the evolution of the plasma in different locations along each strand. Therefore, we obtained light curves in the two EUV channels with regular spacing along the loop. We realised that the model predicts well-defined trends of brightness fluctuations as we move along a loop made of pulse-heated strands. In the channel sensitive to hotter plasma the fluctuations decrease from the top to the bottom of the loop. In the "cooler" channel, they decrease from the bottom to the top. The measurable fluctuations are ultimately caused by the few largest heat pulses, which determine peaks of emission at high temperature at the loop top. The same events propagate to the bottom as peaks at lower temperature. We checked this prediction through the observation and found an excellent quantitative agreement at some positions in the active region core and a widespread presence of this effect through complementary patterns of fluctuations throughout the active region: we see larger fluctuations close to the loop tops in the 94 Å images and close to the loop footpoints in the 335 Å channel.

This result provides a new tool that might be used in the future to diagnose impulsive heating throughout the solar disk from EUV observations. On the other hand, our approach provides interesting constraints to more detailed and self-consistent magneto-hydrodynamic loop models that address the interaction of the plasma with the ambient magnetic field and the conversion of magnetic energy into heat.

# Appendix A

# Emission measure

The coronal plasma is mostly optically thin. The emitted intensity and the dected one along the line of sight are respectively:

$$I_{EM} = \int n^2 P(T) dV \tag{A.1}$$

$$I_{DEC} = \int n^2 G(T) dV \tag{A.2}$$

where n is the density, V is the emitting volume, G(T) is the instrumental response function and P(T) is the plasma emissivity that depends on its chemical composition (e.g., Rosner et al. 1978).
For an isothermal plasma the equation (A.1) will become:

$$I_{EM} = P(T) \int n^2 dV \tag{A.3}$$

in which $\int n^2 dV$ is the emission measure.

# Bibliography


Antiochos, S. K. 1979, ApJ, 232, L125

Antiochos, S. K., MacNeice, P. J., Spicer, D. S., & Klimchuk, J. A. 1999, ApJ, 512, 985

Antiochos, S. K. & Sturrock, P. A. 1976, Sol. Phys., 49, 359

Antolin, P. & Rouppe van der Voort, L. 2012, ApJ, 745, 152

Antonucci, E., Dodero, M. A., Martin, R., et al. 1993, ApJ, 413, 786

Antonucci, E., Dodero, M. A., Peres, G., Serio, S., & Rosner, R. 1987, ApJ, 322, 522

Aschwanden, M. J. & Parnell, C. E. 2002, ApJ, 572, 1048

Aschwanden, M. J., Wuelser, J.-P., Nitta, N. V., Lemen, J. R., & Sandman, A. 2009, ApJ, 695, 12

Bartoe, J.-D. F., Brueckner, G. E., Purcell, J. D., & Tousey, R. 1977, Appl. Opt., 16, 879

Bazarghan, M., Safari, H., Innes, D. E., Karami, E., & Solanki, S. K. 2008, A&A, 492, L13

Benz, A. O. & Krucker, S. 1998, Sol. Phys., 182, 349

Berger, T. E., de Pontieu, B., Fletcher, L., et al. 1999, Sol. Phys., 190, 409

Betta, R., Peres, G., Reale, F., & Serio, S. 1997, A&AS, 122, 585

Betta, R. M., Peres, G., Reale, F., & Serio, S. 2001, A&A, 380, 341

Beveridge, C., Longcope, D. W., & Priest, E. R. 2003, Sol. Phys., 216, 27

Boerner, P., Edwards, C., Lemen, J., et al. 2012, Sol. Phys., 275, 41

Boerner, P. F., Testa, P., Warren, H., Weber, M. A., & Schrijver, C. J. 2014, Sol. Phys., 289, 2377

Bradshaw, S. J. & Cargill, P. J. 2006, A&A, 458, 987

Bradshaw, S. J. & Cargill, P. J. 2013, ApJ, 770, 12

Bradshaw, S. J., Klimchuk, J. A., & Reep, J. W. 2012, Astrophys. J., 758, 53

Bradshaw, S. J. & Mason, H. E. 2003, A&A, 407, 1127

Brooks, D. H., Warren, H. P., & Ugarte-Urra, I. 2012, ApJ, 755, L33

Brooks, D. H., Warren, H. P., Ugarte-Urra, I., & Winebarger, A. R. 2013, ApJ, 772, L19

Brosius, J. W., Daw, A. N., & Rabin, D. M. 2014, ApJ, 790, 112

Brown, J. C. 1973, Sol. Phys., 29, 421

Cargill, P. J. 1993, Sol. Phys., 147, 263

Cargill, P. J. 1994, ApJ, 422, 381

Cargill, P. J. 2014, ApJ, 784, 49

Cargill, P. J., Bradshaw, S. J., & Klimchuk, J. A. 2012, ApJ, 752, 161

Cargill, P. J. & Klimchuk, J. A. 1997, ApJ, 478, 799

Cargill, P. J. & Klimchuk, J. A. 2004, ApJ, 605, 911

Cargill, P. J., Warren, H. P., & Bradshaw, S. J. 2015, Royal Society of London Philosophical Transactions Series A, 373, 40260

Caspi, A., Warren, H., McTiernan, J., & Woods, T. N. 2015, in AAS/AGU Triennial Earth-Sun Summit, Vol. 1, AAS/AGU Triennial Earth-Sun Summit, 20403

Cheng, C.-C., Oran, E. S., Doschek, G. A., Boris, J. P., & Mariska, J. T. 1983, ApJ, 265, 1090

Cirtain, J. W., Golub, L., Winebarger, A. R., et al. 2013, Nature, 493, 501

Craig, I. J. D., McClymont, A. N., & Underwood, J. H. 1978, A&A, 70, 1

Culhane, L., Harra, L. K., Baker, D., et al. 2007, PASJ, 59, 751

De Groof, A., Berghmans, D., van Driel-Gesztelyi, L., & Poedts, S. 2004, A&A, 415, 1141

Delaboudinière, J.-P., Artzner, G. E., Brunaud, J., et al. 1995, Sol. Phys., 162, 291

Di Giorgio, S., Reale, F., & Peres, G. 2003, A&A, 406, 323

Di Matteo, V., Reale, F., Peres, G., & Golub, L. 1999, A&A, 342, 563

Domingo, V., Fleck, B., & Poland, A. I. 1995, Sol. Phys., 162, 1

Doschek, G. A., Boris, J. P., Cheng, C. C., Mariska, J. T., & Oran, E. S. 1982, ApJ, 258, 373

Fisher, G. H., Canfield, R. C., & McClymont, A. N. 1985, ApJ, 289, 414

Fletcher, L. & de Pontieu, B. 1999, in Bulletin of the American Astronomical Society, Vol. 31, American Astronomical Society Meeting Abstracts #194, 963

Foukal, P. 1975, Sol. Phys., 43, 327

Foukal, P. V. 1976, ApJ, 210, 575

Gan, W. Q., Zhang, H. Q., & Fang, C. 1991, A&A, 241, 618

Gburek, S., Sylwester, J., Kowalinski, M., et al. 2013, Sol. Phys., 283, 631

Giacconi, R., Reidy, W. P., Zehnpfennig, T., Lindsay, J. C., & Muney, W. S. 1965, ApJ, 142, 1274

Gold, T. 1964, NASA Special Publication, 50, 389

Golub, L., Deluca, E., Austin, G., et al. 2007, Sol. Phys., 243, 63

Golub, L. & Herant, M. 1989, in Society of Photo-Optical Instrumentation Engineers (SPIE) Conference Series, Vol. 1160, X-Ray/EUV Optics for Astronomy and Microscopy, ed. R. B. Hoover, 629–635

Golub, L. & Pasachoff, J. M. 2009, The Solar Corona

Gomez, D. O., Martens, P. C. H., & Golub, L. 1993, ApJ, 405, 767

Guarrasi, M., Reale, F., Orlando, S., Mignone, A., & Klimchuk, J. A. 2014, A&A, 564, A48

Guarrasi, M., Reale, F., & Peres, G. 2010, ApJ, 719, 576

Handy, B. N., Acton, L. W., Kankelborg, C. C., et al. 1999, Sol. Phys., 187, 229

Hansteen, V. 1993, ApJ, 402, 741

Hara, H., Tsuneta, S., Lemen, J. R., Acton, L. W., & McTiernan, J. M. 1992, PASJ, 44, L135

Harrison, R. A., Sawyer, E. C., Carter, M. K., et al. 1995, Sol. Phys., 162, 233

Haykin, S. 1999, Neural Networks: A Comprehensive Introduction (Prentice Hall)

Hood, A. W. & Priest, E. R. 1979, A&A, 77, 233

Hood, A. W. & Priest, E. R. 1980, A&A, 87, 126

Hudson, H. S. 1991, Sol. Phys., 133, 357

Ignatiev, A. P., Kolachevsky, N. N., Korneev, V. V., et al. 1998, in Society of Photo-Optical Instrumentation Engineers (SPIE) Conference Series, Vol. 3406, Current Russian Research in Optics and Photonics: New Methods and Instruments for Space- and Earth-based Spectroscopy in XUV, UV, IR, and Millimeter Waves, ed. I. I. Sobelman & V. A. Slemzin, 20–34

Jakimiec, J., Sylwester, B., Sylwester, J., et al. 1992, A&A, 253, 269

Judge, P. G., Hansteen, V., Wikstøl, Ø., et al. 1998, ApJ, 502, 981

Kaiser, M. L., Kucera, T. A., Davila, J. M., et al. 2008, Space Sci. Rev., 136, 5

Katsukawa, Y. & Tsuneta, S. 2001, ApJ, 557, 343

Klimchuk, J. A. 2006, Sol. Phys., 234, 41

Klimchuk, J. A. 2015, Royal Society of London Philosophical Transactions Series A, 373, 40256

Klimchuk, J. A., Patsourakos, S., & Cargill, P. J. 2008, ApJ, 682, 1351

Ko, Y.-K., Doschek, G. A., Warren, H. P., & Young, P. R. 2009, ApJ, 697, 1956

Kosugi, T., Matsuzaki, K., Sakao, T., et al. 2007, Sol. Phys., 243, 3

Kramar, M., Jones, S., Davila, J., Inhester, B., & Mierla, M. 2009, Sol. Phys., 259, 109

Krieger, A. S. 1978, Sol. Phys., 56, 107

Lemen, J. R., Title, A. M., Akin, D. J., et al. 2012, Sol. Phys., 275, 17

Levine, R. H. 1974, ApJ, 190, 457

Lin, R. P., Schwartz, R. A., Kane, S. R., Pelling, R. M., & Hurley, K. C. 1984, ApJ, 283, 421

López Fuentes, M. C., Klimchuk, J. A., & Démoulin, P. 2006, ApJ, 639, 459

Lu, E. T. & Hamilton, R. J. 1991, ApJ, 380, L89

MacNeice, P. 1986, Sol. Phys., 103, 47

Martens, P. C. H., Kankelborg, C. C., & Berger, T. E. 2000, ApJ, 537, 471

McTiernan, J. M. 2009, ApJ, 697, 94

Mendoza-Briceño, C. A., Erdélyi, R., & Di G. Sigalotti, L. 2002, ApJ, 579, L49

Miceli, M., Reale, F., Gburek, S., et al. 2012, A&A, 544, A139

Mitra-Kraev, U. & Benz, A. O. 2001, A&A, 373, 318

Montana, D. 1992, in Advances in Neural Information Processing Systems 4 (Morgan Kaufmann), 1110–1117

Müller, D. A. N., Hansteen, V. H., & Peter, H. 2003, A&A, 411, 605

Müller, D. A. N., Peter, H., & Hansteen, V. H. 2004, A&A, 424, 289

Nagai, F. 1980, Sol. Phys., 68, 351

Nagai, F. & Emslie, A. G. 1984, ApJ, 279, 896

Narain, U. & Ulmschneider, P. 1996, Space Sci. Rev., 75, 453

Ofman, L. & Wang, T. 2002, ApJ, 580, L85

Ogawara, Y., Takano, T., Kato, T., et al. 1991, Sol. Phys., 136, 1

Oraevsky, V. N. & Sobelman, I. I. 2002, Astronomy Letters, 28, 401

O'Shea, E., Banerjee, D., & Doyle, J. G. 2007, A&A, 475, L25

Pallavicini, R., Peres, G., Serio, S., et al. 1983, ApJ, 270, 270

Parker, E. N. 1983, in NASA Conference Publication, Vol. 228, NASA Conference Publication, 23–32

Parker, E. N. 1988, ApJ, 330, 474

Parnell, C. E. 2004, in ESA Special Publication, Vol. 575, SOHO 15 Coronal Heating, ed. R. W. Walsh, J. Ireland, D. Danesy, & B. Fleck, 227

Parnell, C. E. & Jupp, P. E. 2000, ApJ, 529, 554

Peres, G. & Reale, F. 1993a, A&A, 275, L13

Peres, G. & Reale, F. 1993b, A&A, 267, 566

Peres, G., Reale, F., & Golub, L. 1994, ApJ, 422, 412

Peres, G., Reale, F., & Serio, S. 1993, in Astrophysics and Space Science Library, Vol. 183, Physics of Solar and Stellar Coronae, ed. J. L. Linsky & S. Serio, 151

Peres, G., Reale, F., Serio, S., & Pallavicini, R. 1987, ApJ, 312, 895

Peres, G., Serio, S., Vaiana, G. S., & Rosner, R. 1982, ApJ, 252, 791

Pesnell, W. D., Thompson, B. J., & Chamberlin, P. C. 2012, Sol. Phys., 275, 3

Peter, H., Bingert, S., Klimchuk, J. A., et al. 2013, A&A, 556, A104

Petralia, A., Reale, F., Testa, P., & Del Zanna, G. 2014, A&A, 564, A3

Priest, E. R. 2011, Journal of Atmospheric and Solar-Terrestrial Physics, 73, 271

Priest, E. R., Foley, C. R., Heyvaerts, J., et al. 2000, Astrophys. J., 539, 1002

Priest, E. R., Heyvaerts, J. F., & Title, A. M. 2002, ApJ, 576, 533

Reale, F. 2014, Living Reviews in Solar Physics, 11, 4

Reale, F., Guarrasi, M., Testa, P., et al. 2011, ApJ, 736, L16

Reale, F., McTiernan, J. M., & Testa, P. 2009a, ApJ, 704, L58

Reale, F., Nigro, G., Malara, F., Peres, G., & Veltri, P. 2005, ApJ, 633, 489

Reale, F. & Orlando, S. 2008, ApJ, 684, 715

Reale, F., Parenti, S., Reeves, K. K., et al. 2007, Science, 318, 1582

Reale, F. & Peres, G. 1995, A&A, 299, 225

Reale, F. & Peres, G. 2000, ApJ, 528, L45

Reale, F., Peres, G., Serio, S., et al. 2000, ApJ, 535, 423

Reale, F., Peres, G., Serio, S., et al. 2000, Astrophys. J., 535, 423

Reale, F., Peres, G., Serio, S., Rosner, R., & Schmitt, J. H. M. M. 1988, ApJ, 328, 256

Reale, F., Serio, S., & Peres, G. 1993, A&A, 272, 486

Reale, F., Testa, P., Klimchuk, J. A., & Parenti, S. 2009b, ApJ, 698, 756

Reep, J. W., Bradshaw, S. J., & Klimchuk, J. A. 2013, ApJ, 764, 193

Reeves, E. M., Timothy, J. G., & Huber, M. C. E. 1977, Appl. Opt., 16, 837

Reidy, W. P., Vaiana, G. S., Zehnpfennig, T., & Giacconi, R. 1968, ApJ, 151, 333

Rosner, R., Tucker, W. H., & Vaiana, G. S. 1978, ApJ, 220, 643

Sakamoto, Y., Tsuneta, S., & Vekstein, G. 2008, ApJ, 689, 1421

Sakamoto, Y., Tsuneta, S., & Vekstein, G. 2009, ApJ, 703, 2118

Scherrer, P. H., Schou, J., Bush, R. I., et al. 2012, Sol. Phys., 275, 207

Schmelz, J. T., Saar, S. H., DeLuca, E. E., et al. 2009, ApJ, 693, L131

Schrijver, C. J. 2001, Sol. Phys., 198, 325

Serio, S., Reale, F., Jakimiec, J., Sylwester, B., & Sylwester, J. 1991, A&A, 241, 197

Shestov, S. V., Kuzin, S. V., Urnov, A. M., Ul'Yanov, A. S., & Bogachev, S. A. 2010, Astronomy Letters, 36, 44

Shimizu, T. 1995, PASJ, 47, 251

Shimizu, T., Tsuneta, S., Acton, L. W., et al. 1994, ApJ, 422, 906

Shimojo, M., Kurokawa, H., & Yoshimura, K. 2002, Sol. Phys., 206, 133

Sigalotti, L. D. G. & Mendoza-Briceño, C. A. 2003, A&A, 397, 1083

Spadaro, D., Lanza, A. F., Lanzafame, A. C., et al. 2003, ApJ, 582, 486

Spitzer, L. 1962, Physics of Fully Ionized Gases

Strong, K. T., Harvey, K., Hirayama, T., et al. 1992, PASJ, 44, L161

Sylwester, B., Sylwester, J., & Phillips, K. J. H. 2010, A&A, 514, A82

Sylwester, B., Sylwester, J., Serio, S., et al. 1993, A&A, 267, 586

Sylwester, J., Gaicki, I., Kordylewski, Z., et al. 1998, in ESA Special Publication, Vol. 417, Crossroads for European Solar and Heliospheric Physics. Recent Achievements and Future Mission Possibilities, 313

Sylwester, J., Kuzin, S., Kotov, Y. D., Farnik, F., & Reale, F. 2008, Journal of Astrophysics and Astronomy, 29, 339

Tajfirouze, E., Reale, F., Petralia, A., & Testa, P. 2015, ApJ, in press

Tajfirouze, E. & Safari, H. 2012, ApJ, 744, 113

Taroyan, Y., Bradshaw, S. J., & Doyle, J. G. 2006, A&A, 446, 315

Teriaca, L., Warren, H. P., & Curdt, W. 2012, ApJ, 754, L40

Terzo, S., Reale, F., Miceli, M., et al. 2011, ApJ, 736, 111

Terzo, S., Tsuneta, S., Kano, R., Miceli, M., & Reale, F. 2010, in COSPAR Meeting, Vol. 38, 38th COSPAR Scientific Assembly, 2898

Testa, P., De Pontieu, B., Allred, J., et al. 2014, Science, 346, 1255724

Testa, P., De Pontieu, B., Martínez-Sykora, J., et al. 2013, ApJ, 770, L1

Testa, P., Drake, J. J., & Landi, E. 2012, ApJ, 745, 111

Testa, P., Peres, G., & Reale, F. 2005, ApJ, 622, 695

Testa, P. & Reale, F. 2012, ApJ, 750, L10

Testa, P., Reale, F., Landi, E., DeLuca, E. E., & Kashyap, V. 2011, ApJ, 728, 30

Tousey, R., Bartoe, J.-D. F., Brueckner, G. E., & Purcell, J. D. 1977, Appl. Opt., 16, 870

Tripathi, D., Mason, H. E., Dwivedi, B. N., del Zanna, G., & Young, P. R. 2009, ApJ, 694, 1256

Tsuneta, S., Acton, L., Bruner, M., et al. 1991, Sol. Phys., 136, 37

Ugarte-Urra, I. & Warren, H. P. 2011, ApJ, 730, 37

Vaiana, G. S., Reidy, W. P., Zehnpfennig, T., van Speybroeck, L., & Giacconi, R. 1968, Science, 161, 564

van Speybroeck, L. P., Krieger, A. S., & Vaiana, G. S. 1970, Nature, 227, 818

Vekstein, G. 2009, A&A, 499, L5

Vernazza, J. E., Avrett, E. H., & Loeser, R. 1981, ApJS, 45, 635

Vesecky, J. F., Antiochos, S. K., & Underwood, J. H. 1979, ApJ, 233, 987

Viall, N. M. & Klimchuk, J. A. 2011, ApJ, 738, 24

Viall, N. M. & Klimchuk, J. A. 2012, ApJ, 753, 35

Viall, N. M. & Klimchuk, J. A. 2013, ApJ, 771, 115

Walsh, R. W. & Ireland, J. 2003, A&A Rev., 12, 1

Warren, H. P., Brooks, D. H., & Winebarger, A. R. 2011, ApJ, 734, 90

Warren, H. P. & Winebarger, A. R. 2007, Astrophys. J., 666, 1245

Warren, H. P., Winebarger, A. R., & Brooks, D. H. 2010a, ApJ, 711, 228

Warren, H. P., Winebarger, A. R., & Brooks, D. H. 2010b, ApJ, 711, 228

Warren, H. P., Winebarger, A. R., & Brooks, D. H. 2012, ApJ, 759, 141

Warren, H. P., Winebarger, A. R., & Hamilton, P. S. 2002, ApJ, 579, L41

Warren, H. P., Winebarger, A. R., & Mariska, J. T. 2003, Astrophys. J., 593, 1174

Widrow, B. & Hoff, M. E. 1960, in Proceedings WESCON, 96–104

Wilhelm, K., Curdt, W., Marsch, E., et al. 1995, Sol. Phys., 162, 189

Winebarger, A. R., Cirtain, J., Golub, L., et al. 2014, ApJ, 787, L10

Withbroe, G. L. & Noyes, R. W. 1977, ARA&A, 15, 363

Woods, T. N., Eparvier, F. G., Hock, R., et al. 2012, Sol. Phys., 275, 115

Zhitnik, I. A., Bugaenko, O. I., Ignat'ev, A. P., et al. 2003, MNRAS, 338, 67